Fractal Characteristics of Ice-Supersaturated Regions in the Tropopause Region of the ~~northern midlatitudes~~Northern Midlatitudes

Helena Schuh[1], Philipp Reutter[1], Stefan Niebler[2], and Peter Spichtinger[1]

[1]Institute for Atmospheric Physics, Johannes Gutenberg University Mainz, Mainz, Germany
[2]Institute for Computer Sciences, Johannes Gutenberg University Mainz, Mainz, Germany

Correspondence: Helena Schuh (hschuh01@students.uni-mainz.de)

Abstract. Ice supersaturated regions (ISSRs) are air masses in the upper troposphere and lower stratosphere (UTLS) where ~~relative humidity with respect to ice (RHi) exceeds 100%~~saturation ratio over ice (S_i) exceeds 1, i.e. regions with enhanced water vapor concentrations. These are potential formation regions of cirrus clouds and contrails. While the impact of cloud free regions of enhanced water vapor on the planetary radiation balance is small to negligible, thin cirrus clouds and aircraft induced contrail cirrus formed within them might have a large radiative impact. Understanding the characteristics of ISSRs, including their geometry and seasonal variability, is essential for improving atmospheric models in representing ice clouds correctly. While ISSR's ~~path-length~~ pathlength statistics, i.e. 1D characteristics, have already been studied, their geometric properties, particularly fractal properties such as self-similarity, and their seasonal variability remain largely unexplored. We identify ISSRs using ERA5 reanalysis data spanning from 2010 to 2020 at three pressure levels. An area-perimeter method is employed to compute fractal dimensions. The results reveal slopes equaling fractal dimensions with high coefficients of determination, strongly suggesting that ISSRs in the UTLS exhibit fractal behavior. A seasonal cycle in ~~both dimension and total count of observed ISSRswas found.~~ total number and area of ISSRs, as well as in the fractal dimension is found, in combination with a strong vertical variation. We hypothesize that this is caused by the seasonal variation of convective and frontal activity. We further analyzed the latitudinal and longitudinal ~~spans of ISSRs and the path lengths~~ extensions of ISSRs as well as the pathlengths of modeled flights along commercial flight routes. The results of ~~the~~ these horizontal extensions are consistent with the fractal properties, and suggest distinct formation processes for ISSRs.

1 Introduction

Ice supersaturated regions (ISSRs) in the upper troposphere and lower stratosphere (UTLS) serve as key environments for the formation and persistence of in situ cirrus clouds. These regions ~~, defined by a relative humidity with respect to ice (RHi) exceeding 100%,~~ occur when the water vapor partial pressure p_v exceeds the water vapor saturation pressure over ice at temperature T~~:~~

$$\mathrm{RH_i} = 100\% \cdot \frac{p_v}{p_{si}(T)} = 100\% \cdot S_i,$$

, leading to a saturation ratio

$$S_i = \frac{p_v}{p_{si}(T)} \tag{1}$$

~~With the saturation ratio S_i~~greater than 1. Ice supersaturation ~~–~~(first described by Alfred ~~Wegener (1911)–~~Wegener (1910, 1911))is a frequent and widespread phenomenon in the UTLS ~~(see, e.g.,~~ (Gierens and Spichtinger, 2000; Spichtinger et al., 2003b; Gettelman et al., 2006; Lamquin et al., 2012; Petzold et al., 2020; Reutter et al., 2020)~~)~~, where the cold and dry conditions render even small variations in humidity highly significant. ISSRs not only serve as a key environment for the formation of in situ cirrus clouds (Krämer et al., 2016), but also as a prerequisite for persistent contrails ~~(Stuber et al., 2006; Lee et al., 2010, 2021), which~~ (Schumann, 1996; Stuber et al., 2006; Lee et al., 2010, 2021); this is nowadays a major topic in the context of contrail avoidance, since these contrails can persist for over 10 hours and spread into contrail cirrus (Haywood et al., 2009). Cloud free ISSRs themselves have a relatively minor direct influence on the local radiation budget, although their transition into cirrus clouds significantly alters radiative forcing (Fusina et al., 2007). ISSRs and cirrus clouds are predominantly found in the upper troposphere, but they can also extend above the tropopause (Spichtinger et al., 2003a; Reutter et al., 2020), ~~affecting~~ affecting the lower stratosphere (LS). The upper troposphere–lower stratosphere (UTLS) region is characterized by extremely cold and dry air masses (Dessler and Sherwood, 2009; Held and Soden, 2000), making outgoing longwave radiation particularly sensitive to ~~absolute changes~~ small relative perturbations in UTLS water vapor~~(Riese et al., 2012)~~, due to the very low background concentrations (Clough et al., 1992); gradients in saturation ratio are closely related to the respective changes in longwave radiation (e.g. Fusina et al., 2007), potentially resulting into local changes of the thermodynamic structure of the tropopause region (Köhler et al., 2024). Consequently, variations in ISSR occurrence and cirrus cloud formation within this region have important implications for climate dynamics and radiative balance (Lee et al., 2010). ISSRs are not necessarily cloud free air masses, although former investigations suggest this property. However, the transition from ice clouds to cloud free air is very smooth and usually there are ~~not~~ no sharp boundaries. In our study we will not further distinguish between clear and cloudy air, ~~we are just~~ as we are interested in the thermodynamic state of the air masses. While studies have examined the horizontal extent of ISSRs using pathlength statistics (Gierens and Spichtinger, 2000; Diao et al., 2014; Spichtinger and Leschner, 2016; Reutter et al., 2020), their two-dimensional spatial characteristics, including shape and scaling behavior, remain poorly understood and ~~was~~ were not studied in detail yet. ~~However, statistical~~ Statistical investigations are challenging because of the ISSRs' variability in size and shape~~, respectively~~. In addition, some metrics must be defined (or even developed) for studying ISSRs as 2D/3D objects, instead of just using point measurements~~The radiative effects~~ . The radiative effects of cirrus clouds, including those related to natural or anthropogenic origins, are a subject of ongoing research. However, this study emphasizes the structural and statistical properties of ISSRs. Understanding their morphology and variability is essential for improving microphysical parameterizations and ~~for~~ interpreting the atmospheric processes that control cloud evolution in the UTLS.

A potential approach in studying the geometric properties of ~~ISSRs~~ 2D or 3D objects is to examine their potential self-similarity, i.e. the fractal properties of these macroscopic objects. In general, fractals are geometric structures characterized by self-similarity. ~~Self-similar~~ These objects exhibit similar patterns on different scales~~. They~~ , and they differ from traditional Euclidean shapes by possessing non-integer (fractional) dimensions that describe ~~how~~ the way their complexity changes with scale ~~(cf. Peitgen et al., 2004). Although ,~~ (Peitgen et al., 2004). Although the whole research field of fractal geometry was defined by Mandelbrot in 1975, and became famous in the ~~1980ies (e.g., Mandelbrot, 1982), there were~~ 1980s (e.g., Mandelbrot, 1982) , investigations on the fractal nature of natural objects were made before Mandelbrot. ~~Actually, Richardson~~ Notably, Richardson (1926) carried out first investigations on the nature of turbulence, addressing already some fractal properties~~(Richardson, 1926)~~. Thus, fractal analysis has a longstanding tradition in atmospheric physics, ~~and~~ especially in cloud physics. In ~~many~~ numerous previous studies, the fractal nature of clouds is investigated, ranging from cumulus cloud statistics and properties (Cahalan and Joseph, 1989; Joseph and Cahalan, 1990; Cahalan et al., 1994; Gotoh and Fujii, 1998; Siebesma and Jonker, 2000), rain and hail clouds (Lovejoy, 1982; Lovejoy and Mandelbrot, 1985; Rys and Waldvogel, 1986), tropical clouds (Benner and Curry, 1998; Batista-Tomás et al., 2016), noctilucent clouds (von Savigny et al., 2011; Brinkhoff et al., 2015), and cloud fields in high resolution models (Christensen and Driver, 2021)~~, respectively. In addition~~. Additionally, fractal analysis is a key technique for turbulence theories and data evaluation ~~(see, e.g., Sreenivasan and Meneveau, 1986; Sreenivasan, 1991)~~ (e.g., Sreenivasan and Meneveau, 1986; Sreenivasan, 1991). In some studies, clouds and turbulence investigations are combined in order to explain fractal properties of clouds by the underlying turbulence (or diffusion) characteristics ~~(see, e.g., DeWitt et al., 2024; Rees~~ ~~. However, ISSRs or cirrus clouds were not investigated in this respect. If~~ (e.g., DeWitt et al., 2024; Rees et al., 2024). Overall, there is strong evidence that clouds at different vertical levels show fractal behavior. Thus, it is reasonable to question whether their potential formation regions, i.e. the ISSRs in case of ice clouds, also exhibit similar properties. If this holds true and ISSRs also display self-similar characteristics, determining their fractal dimension can provide insight into their spatial attributes and characteristics. In addition, these properties should be represented in models on different scales; thus, such properties might serve as indication for correct representation of ISSRs and cirrus in model ~~parameterisations~~parameterizations.

To identify and study ISSRs, we analyze ERA5 reanalysis data that incorporates absolute humidity, temperature and pressure ~~and distinguish between ice sub- and supersaturated air masses~~ in terms of ice supersaturation. For the investigation we distinguish water vapor in air masses in the state of sub or super saturation with respect to ice by applying a threshold of $S_{i,\mathrm{threshold}} = 0.9$, already taking into account the dry bias of ERA5 in the tropopause region (Reutter et al., 2020). A grid point with values $S_i < S_{i,\mathrm{threshold}}$ is marked as subsaturated (index=0), and grid points with values $S_i \geq S_{i,\mathrm{threshold}}$ are counted as supersaturated (i.e. ISSR, index=1). As a result a simplified binary representation of these regions ~~is obtained. Applying a definition for connection on gridded data we determine ISSRs as connected areas~~ on the grid is obtained and connected areas are identified and determined as ISSRs. Based on this consideration the actual areas and perimeters of ISSRs are calculated to accurately describe their shapes. ~~We take also into account the effects of Earth's curvature and the uneven distribution of grid points. To asses the fractal characteristics~~ For a gridded data set, the spatial resolution is inherently limited; therefore, a rigorous derivation of a fractal dimension is not feasible. However, to assess the the fractal characteristics, and especially the self-similarity of ISSRs, we examine the area-perimeter relation. ~~Plotting the measured area against the~~

~~perimeter~~ A scatter plot of measured perimeters against the areas of individual ISSRs on logarithmic scales ~~shows linear behaviour~~ reveals a linear relationship with slope α, ~~constituting the fractal dimension~~which can be interpreted as the fractal (or self-similar) dimension $D = 2\alpha$. This analysis provides ~~us~~ a quantitative measure of the macroscopic ~~objects. This has~~ structures and has important implications for further investigations. ~~By exploring and quantifying the self-similarity as a fractal characteristic of these regions and assigning them a dimension we may refine atmospheric modelsand improve representations of high-altitude ISSRs . More accurate geometric characterizations of ISSRs could enhance climate models , improve weather forecasting, and optimize aviation routing to mitigate contrail formation. Enhanced accuracy and precision in our understanding of atmospheric phenomena, coupled with streamlined and efficient computational processes, may lead to improved models for weather forecasting, climate prediction and contrail avoidance~~The derived fractal properties of ISSRs might be helpful for the evaluation of atmospheric models, since for a correct representation of ISSRs in weather and climate models the self-similar properties should be comparable. For instance, forecasts of ISSRs in terms of contrail avoidance (e.g. Petzold et al., 2025) must represent the fractal nature of these regions. Thus, our results could serve as a meaningful test of models regarding the representation of ice supersaturation in the UTLS.

The study is structured as follows~~.~~: In Sec. 2 the data set and the methods are introduced. In Sec. 3 the fractal characteristics of ISSRs as found in the data are investigated. This is followed in Sec. 4 by the investigation on the horizontal ~~span~~ extension of ISSRs. The results are discussed in Sec. 5.2 and conclusions are drawn in Sec. 5.1.

2 Data and Methods

In this section we present the data set and describe the methods used for the investigation of the data.

2.1 Data set ERA5

The study ~~utilizes~~ analyzes eleven years of ERA5 reanalysis data (Hersbach et al., 2020) covering the period from January 1, 2010, to December 31, ~~2020 (i.e. full 11 years of data).~~ 2020. Data is available at the standard synoptic times each day (0, 6, 12, 18 UTC), resulting in a total of 16,060 datasets for analysis. ERA5 provides data with a horizontal resolution of 0.25 degrees in longitude and latitude, ~~respectively. The~~ and a vertical resolution of 137 model levels with an approximate resolution in the tropopause region of about 300 m. The data set contains variables of 3D winds (u, v, w), temperature T, and specific humidity q. The geographical area used for the analysis is narrowed down to range from 80 to 30 degrees latitude in the Northern hemisphere in order to exclude the tropics and polar regions. In our investigation we focus on pressure levels of 200 hPa, 250 hPa, and 300 hPa, representing the upper troposphere and tropopause region (similarly to the investigation by Lamquin et al., 2012); the data on adjacent model levels were interpolated on the respective isobaric surfaces.

2.2 Methods

~~The first objective in~~ Here, we briefly describe the processing of the data~~is the identification and localization of ISSRs on the respective pressure levels. The defining order parameter of an ISSR is a saturation ratio S_i that exceeds 1. The saturation ratio S_i is calculated using the specific humidity q, temperature T and pressure p as~~; for details we refer to appendix A.

2.2.1 Relevant variable

The thermodynamic order parameter for ISSRs is the saturation ratio

$$S_i = \frac{p \cdot q}{\epsilon \cdot p_{si}(T)} = \frac{p_v}{p_{si}(T)} \tag{2}$$

as calculated from the ERA5 variables p, T, q, using the ratio of molar masses of water and air, ~~respectively, i.e.~~

$$\cancel{\epsilon = \frac{M_v}{M_d}}$$

i.e. $\epsilon = \frac{M_v}{M_d}$ and the saturation vapour pressure over (hexagonal) ice p_{si} in the formulation by Murphy and Koop (2005), i.e.,

$$p_{si} = \exp\left(9.5504 - \frac{5723.265}{T} + 3.53068\log(T) - 0.00728332\,T\right), \tag{3}$$

~~which is~~ Here, T is given in Kelvin and p_{si} is obtained in Pascal; the formulation is valid for temperatures $T > 100$ K. ~~Specific humidity and temperature are accessible as variables in ERA5 data for various pressure levels. As such, the pressure p is provided as well.~~

~~The identification of ISSRs requires a threshold defining supersaturation; actually, this threshold is given by the~~ The thermodynamic equilibrium between vapor and ice ~~, which would be $S_c = 1$.~~ is given by $S_i = 1$.
However, since ERA5 data underestimate the humidity in the UTLS region ~~(cf. Köhler et al., 2024; Reutter et al., 2020)~~(Köhler et al., 2024
, we choose a threshold value of ~~$S_c = 0.9$.~~ $S_{i,\text{threshold}} = 0.9$. Note that we use no further information about possible clouds inside the ISSRs. A data point is assigned to be supersaturated (~~or belongs~~ i.e. belonging to an ISSR) if ~~$S_i \geq S_c = 0.9$~~$S_i \geq S_{i,\text{threshold}} = 0.9$
Using this criterion we create ~~for each pressure level~~ a two dimensional binary field with subsaturated data points (index = 0) and data points inside an ISSR (index = 1) ~~. After identifying the ISSRs on their respective pressure levels, the binary fields are further processed to be prepared for the measuring processes.~~

~~Since we are interested in ISSRs as macroscopic objects consisting of many data points,~~ for each pressure level. For a macroscopic object we have to specify ~~which data points are connected, hence forming an ISSR as an island of points~~ a measure for the connectivity of single data points (with index = 1~~on the respective~~) on the gridded isobaric surface. ~~In figure A1 two possible definitions of neighborhoods of points on gridded data are shown, originating from investigations with cellular automaton (cf. Chopard and Droz, 1998). In case of a 4-neighborhood (or von Neumann neighborhood), the central pixel has only connection to pixels via the four edges of the point, whereas in case of a~~ We choose the 8-neighborhood (or Moore neighborhood)~~the~~ , i.e. a central pixel is ~~additionally connected to~~ connected to the neighboring pixels via the ~~diagonals~~[1]~~. We~~

[1]~~In the description of the used program package, the 4-neighborhood is called 1-connectivity, and the 8-neighborhood is called 2-connectivity. Actually, in literature these terms are not frequently used.~~

~~decided to use the Moore neighborhood for connecting data points as ISSRs, since it seems to be a more physical measure for connecting pixels. However, the definition of connectivity (or equivalently a certain neighborhood) influences the resulting islands of connected pixels and thus number, perimeter and area of resulting ISSRs. Actually, the 8-neighborhood avoids too small areas, which seems to be plausible for our investigations.~~

~~In order to differentiate individual ISSRs and correctly correlate areas and perimeters later, the contiguous binary islands are labeled with non-zero integers counting up from one. Each ISSR is thus allocated a unique number allowing identification by value iteration over ISSRs in the following processes.~~

~~In our investigation~~ edges and the diagonals. This definition, originating from investigations with cellular automaton (Chopard and Droz, , is essential, since the connectivity of a physical object should not (or as little as possible) depend on the orientation of a grid. A visualization of the Moore neighborhood is represented in appendix A. For a substantial analysis, we consider only ISSRs consisting of at least $N = 24$ pixels, i.e. exceeding a minimum size; otherwise, a possible self-similar structure would not be reliably resolved. Here, we follow the recommendation by Christensen and Driver (2021). Furthermore, we concentrate on the midlatitudes in the Northern Hemisphere ~~. However, ISSRs might extend to~~ ($30 - 80°$N). As ISSRs may extend into polar or tropical regions~~. Thus, we have to specify a criterion for counting ISSRs. All ISSRs crossing the margins of 80 and 30 degrees latitude are deleted (i.e. the index is set to~~ , we exclude those objects crossing the boundaries of 30°N and 80°N (setting the index = 0) ~~instead of being cut off to avoid skewed results concerning area and perimeter .~~ to avoid artificialyl smoothing perimeter and cropping area. For the further evaluation, the resulting connected binary islands (i.e the ISSRs) are numbered.

2.3 ~~Measuring Island Area~~

~~One main challenge in measuring ISSR properties is the distortion caused by the curvature of the Earth and the geographical grid.The distances between neighboring points depends on their position in the grid on a sphere. The area of a pixel decreases with increasing proximity to the pole. In order to assign an area to an ISSR, each pixel needs to be allocated a corresponding area in square meters depending on its position in~~

2.2.1 Measuring Island Area and Perimeter

The ISSRs are located on the geographical grid ~~. The coordinate points themselves are not the vertices of each quadrilateral area but their centers. The data points with coordinates (x, y) being spaced in 0.25 degree intervals results in the vertices $v_1 = (x - 0.125, y + 0.125)$, $v_2 = (x - 0.125, y - 0.125)$, $v_3 = (x + 0.125, y - 0.125)$, $v_4 = (x + 0.125, y + 0.125)$, as visualized in figure ??.~~

~~In pursuance of the assigning of areas for individual pixels, an array with the same dimensions as those of the data arrays is created. The elements of the two dimensional array represent the quadrilateral areas around the coordinate corresponding to~~ of the ~~position in the array. Plugging in the coordinates of each data point for x and y the vertices, the real area is calculated using the Python package `pyproj.Geod` (Snow et al., 2025). Each element in the array of labeled islands has an assigned area~~ Earth. Since we use a latitude-longitude description we have to take into account the distortion caused by the curvature of the Earth. Each grid point can be seen as the center of an almost quadratic pixel with a respective area (in square meters~~.~~

~~Iterating over the label values, the areas corresponding to the position of the values are added up. The sum equals the total area of the ISSR.~~

2.3 ~~Measuring Island Perimeter~~

~~Similar challenges as for the determination of one grid point's area are present in measuring the perimeter of ISSRs due to the curvature of the Earth and the grid distortion. Contrary to the areas, the Python tools~~), which can be assigned by using the Python package `pyproj.Geod` ~~for measuring perimeters are not suitable for determining the perimeter of an entire labeled island. The input would have to entail the border pixels only and sort them in a clockwise or anticlockwise direction. The perimeter of holes in the island would not be included. Lastly, the algorithm calculates the perimeterby connecting the pixels center points, which leads to an underestimated perimeter, as depicted in Figure **??**.~~

~~This issue was addressed by calculating the real length in meters for each of the four edges of the quadrilateral areas surrounding the data points. Analogous to the process of determining the real areas, an array in the same shape as the data on a pressure level was created. Each element is a list with four elements representing the length of the four sides (figure **??**)~~

~~The~~ (Snow et al., 2025). For the calculation of the perimeter~~is calculated iterating over the values of the island labels. For each value and island, it is first verified whether a pixel is a border pixel that needs to be considered in the perimeter calculations. The value of each pixel adjacent to one of the four sides is examined to determine if it is zero; in this case a border pixel is found. The corresponding length for the position in the two dimensional array and the side bordering a zero value is added to a perimeter sum. Utilizing this approach enables the measurement of both~~, we had to develop an additional tool, taking into account the length of the respective boundaries of the pixel without a neighboring pixel. The overall perimeter of the labeled island is calculated iteratively; here, we can determine both, internal and external borders. ~~One has to mention here~~ It should be noted that this method leads to a ~~slight~~ minor overestimation of perimeter values for ~~a gridded object~~ gridded objects as compared to ~~the analytical manifold~~their real (potentially smooth) counterparts, as represented on a grid. This issue is discussed in appendix ~~**??**.~~ D. Further details of the method can be found in appendix A.

2.3 ~~Calculation of the Fractal Dimension~~

2.2.1 Calculation of the Fractal Dimension

~~The most special property~~ A key characteristic of fractals is self-similarity, ~~which manifests itself in a new~~ the defining property upon which we base our approach for the dimension of ~~the~~ objects. The fractal dimension most commonly refers to the Hausdorff dimension~~, which goes beyond the demands and aims~~ ; however, its rigorous determination lies beyond the scope of this work. The general concept ~~would be to enhance the~~ involves progressively increasing the spatial resolution of the data, i.e.~~zooming into smaller distances and measuring the length (or even area, volume etc.) using subsequently smaller unit circles, spheresand so on~~ examining smaller length scales and measuring geometric properties (such as length, area, or volume) using successively smaller measuring elements (e.g. circles or spheres). In the limit of this sequence ~~we obtain~~ the so-called Hausdorff dimension is obtained, which is a positive real number $\cancel{D_H \in \mathbb{R}}$ $D_H \in \mathbb{R}_+$ (Peitgen et al., 2004). As a consequence, the perimeter of fractal objects ~~become~~ diverges and tends to infinity in the limit. ~~Often, this procedure cannot be carried out for real data , also because of the distinct resolution, as in our case of gridded ERA5 data and no possibility to enhance the resolution~~ This procedure is often not feasible for real-world data due to the finite resolution, in particular for gridded data sets such as ERA5, where the resolution is fixed and cannot be refined arbitrarily.

Consequently, a different method is employed to calculate the dimension for data in ~~two-dimension~~two-dimensions. For this purpose, the area-perimeter relation is investigated. This ~~kind~~ type of relationship was introduced by Lovejoy (1982) to study fractal properties of clouds and rain areas, i.e. the self-similarity of such objects. It is defined as follows: ~~we assume that there is~~ a power law relationship between the ~~area A and the~~ perimeter P and the area A of a two dimensional object ~~such that~~ is assumed, such that

$$\cancel{A}P = C \cdot \cancel{P^{\alpha} \Leftrightarrow} A^{\frac{D}{2}} \Longleftrightarrow \log(\cancel{A}P) = \log(C) + \cancel{\alpha}\frac{D}{2}\log(\cancel{P}A) \qquad (4)$$

with C a scaling parameter. Thus, using scatter plots of data points ~~(P, A)~~ (A, P) in a double logarithmic scale, the ~~area~~ perimeter shows a linear behavior with respect to the ~~perimeter~~ area with a slope α, which is not necessarily ~~a natural number (i.e. 2 as expected from geometry)~~ an integer number but rather a non-negative real number $\alpha \in \mathbb{R}$. ~~For two dimensional objects as~~ This can be used for calculating the "fractal" dimension $D = 2 \cdot \alpha$. For regular geometric objects we would obtain a value $D = 1$ (see also the discussion in appendix B); however, for planar, fractal objects as e.g. ISSRs on a isobaric surface we assume ~~$1 \leq \alpha \leq 2$~~ $1 < D < 2$. The value of ~~α~~ D can be determined by linear fit ~~. Note, that our definition is somewhat different to other evaluations (e.g. Batista-Tomás et al., 2016). Often, the perimeter-area relation is defined as $P = \tilde{C} \cdot A^{\frac{D}{2}}$ with the constant D termed as fractal dimension; of course, both exponents can be related by $\alpha = \frac{2}{D}$. Since with Eq. (4) the dimensional relation between length and area, as well as the deviation from the usual dimension, is more obvious, we stay with this definition.~~ with slope α.

As observed by Cheng (1995), the "dimension" ~~α~~ D as derived by the area-perimeter relation does not agree with the Hausdorff dimension in general. This raises the question if the use of this relation and thus the obtained value ~~α~~ D is meaningful at all. However, this method is ~~quite~~ frequently employed to ascertain fractal dimensions and analyze the respective objects. Already Mandelbrot et al. (1984) found that the dimension ~~α as~~ D obtained by area-perimeter relations ~~agree~~ agrees with fractal dimensions ~~as~~ obtained by spectral analysis. Sakellariou et al. (1991) also discussed this issue, and ~~finally~~ concluded that the method is "the most stable and least ambiguous method" for obtaining fractal dimensions. In Klinkenberg (1994) ~~also~~ other methods for determining fractal dimensions are reviewed. While the dimension ~~α~~ D calculated using the area-perimeter relation (Eq. (4)) does not satisfy the mathematical definition of the fractal dimension, it is appropriate to use this approach in order to study the fractal characteristics and properties of phenomena. As these naturally occurring phenomena are not perfect fractals, a pragmatic approach such as the area-perimeter relation is sufficient for a ~~meaningful evaluation.~~ relevant evaluation. Finally, Florio et al. (2019) showed that for island-type objects, such as our ISSRs, the area-perimeter approach is meaningful and results into dimensions close to the classical fractal dimensions.

The area-perimeter relation and variations of it ~~has~~ have been used in many applications, as e.g. to study the fractal characteristics of rain and cloud areas ~~(Lovejoy, 1982)~~(Lovejoy, 1982; Lovejoy and Mandelbrot, 1985), to determine the fractal perimeter dimension of noctilucent clouds (von Savigny et al., 2011), to measure the fractal structure of interstellar clouds (Vogelaar and Wakker, 1994), and to classify tropical clouds by their fractal dimension (Batista-Tomás et al., 2016).

For the ERA5 data in this study (as for all gridded data), the perimeter ~~can not~~ cannot approach infinity as the horizontal resolution limits the frayed nature of the ISSRs' perimeter, further justifying the employment of the area-perimeter method. The dimension calculated with the area-perimeter method will hereafter be referred to as the fractal dimension. As ISSRs have irregular boundaries, the dimension is expected to be in the range ~~$1 < \alpha < 2$~~ $1 < D < 2$. In appendix B we exemplarily show how the fractal dimension might change by either changing the shape of ~~ellipses~~ rectangulars systematically or fraying the boundary of squares.

For gridded data, area and perimeter can only be approximated. Possible errors are underestimation of the area and overestimation of the perimeter, as discussed in Sanchez et al. (2005) and Imre (2006). In appendix D we investigate these issues ~~in case of spheres. However, the analysis makes us confident~~ for spheres. The analysis indicates that the quality of the evaluation is not ~~affected and thus the~~ compromised. The derived fractal dimensions (i.e. exponents in Eq. (4)) ~~are~~ can therefore be regarded as robust estimates and ~~can be used~~ are suitable for further, ~~even~~ including quantitative, analysis.

3 Fractal properties of ISSRs

In this section we investigate the fractal properties of ISSRs~~. In addition~~, i.e. the derived fractal dimension D. Subsequently, more standard properties, such as the number and area of ISSRs, as well as their seasonal and annual evolution are investigated.

3.1 ISSR Number Count and Area

Figure~~1 shows~~ 1 shows the number of observed ISSRs by month on the 200 hPa, 250 hPa and 300 hPa pressure levels ~~in the timespan~~ during the period from 2010 to 2020. The total number is a sum of all ISSRs appearing at each point in time. This causes the number to be significantly higher than the ISSRs that appeared in a given month, as ISSRs are counted multiple times when having a ~~lifespan longer that~~ lifespan longer than 6 hours. A clear dependence of the number of ISSRs with ~~height is visible~~altitude is evident. At lower altitudes (i.e. higher pressures) we find ~~much~~ significantly more ISSRs than at higher altitudes. This can be explained by the fact that in the extratropics the (thermal) tropopause is located in the pressure range between 300 and 200 hPa, and ISSRs are almost exclusively located in the troposphere; only few ISSRs seem to reach into the stratosphere (Spichtinger et al., 2003a). Generally, ISSRs are most ~~frequent~~ frequently located close to the tropopause. ~~Actually, the~~ The tropopause also shows a seasonal cycle with high altitudes during summer and lower altitudes during winter ~~, respectively~~(e.g., Spichtinger et al., 2003a). Nevertheless, the probability to measure dry and warm air in the stratosphere at a certain pressure level in the extratropics is much higher for pressure level $p = 200\,\mathrm{hPa}$, than for $p = 250\,\mathrm{hPa}$ or $p = 300\,\mathrm{hPa}$~~, respectively~~. This might explain the strong differences in the amount of ISSRs between the three pressure levels. The strong seasonal cycle in the number of ISSRs is a prominent feature, which is most pronounced at pressure level $p = 300\,\mathrm{hPa}$, i.e. in the upper troposphere. We find maxima in summer and minima in winter for all 3 pressure levels. The month with the highest observed number at pressure level ~~$p = 300\mathrm{hPa}$~~ $p = 300\,\mathrm{hPa}$ is July 2013 with ~~18230~~ 9511 detected ISSRs, ~~whereas~~

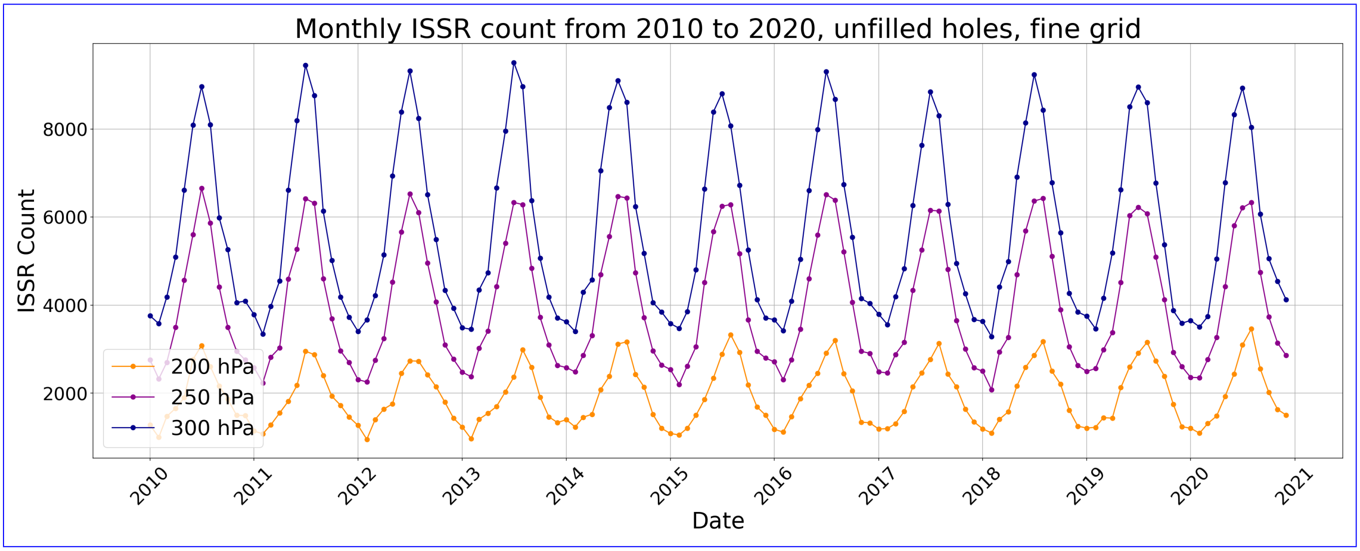

Figure 1. ISSR Number count in each month from 2010 to 2020 at pressure levels 200 hPa (orange), 250 hPa (violet) and 300 hPa (dark blue); here, the data in the ERA5 resolution is used, possible holes in the ISSRs are not filled.

the minimum number of 3290 ISSRs at the same pressure level ~~with 5591~~ can be observed in February 2018. Respectively, the highest number of ISSRs at pressure level ~~$p = 200\mathrm{hPa}$~~ $p = 200\,\mathrm{hPa}$ was recorded in ~~May 2018 with 6257~~ July 2020 with 3462 ISSRs, whereas the minimum was observed in February 2012 with ~~1434~~ 954 ISSRs. Here, we see the ~~huge~~ substantial spread in the amount of ISSRs.

The seasonal cycle compares well with former investigations. Spichtinger and Leschner (2016) also found this signature with highest values of ISSR numbers during summer and lowest counts in the winter's season. Furthermore, the strong variation of numbers with the vertical levels agrees also well with our findings.

In addition to the total number of ISSRs we investigate the total area of the detected ISSRs. As for the number of ISSRs, in Figure 2 the total area of observed ISSRs by month on the 200 hPa, 250 hPa and 300 hPa pressure levels in the timespan from 2010 to 2020 is shown. As for the evaluation of the total number, the area might be enhanced by counting long-lived ISSRs multiple times. The total area is largest at the lowest altitude (i.e. pressure level $p = 300\,\mathrm{hPa}$), and is decreasing with increasing altitude. The highest total area in one month was observed in May 2019 with a summed area of $2.65 \cdot 10^9\mathrm{km}^2$ at pressure level $p = 300\,\mathrm{hPa}$. On the same pressure level the minimum of $1.32 \cdot 10^9\mathrm{km}^2$ is found in February 2018. At the highest altitude level (pressure level $p = 200\,\mathrm{hPa}$) the area is strongly reduced as compared to the other two levels, which have comparable area values. At $p = 200\,\mathrm{hPa}$ the month with the highest total area of supersaturation in respect to ice is July 2020, summing up to $1.12 \cdot 10^9\mathrm{km}^2$. February 2015 at this pressure level constitutes the absolute minimum observed on all pressure levels with $0.41 \cdot 10^9\mathrm{km}^2$. Analogous to the total number, the area also shows a seasonal cycle, although it is not as strongly pronounced. We find maximum values in the summer months, and minimum values in the winter months, similarly to the investigations of the

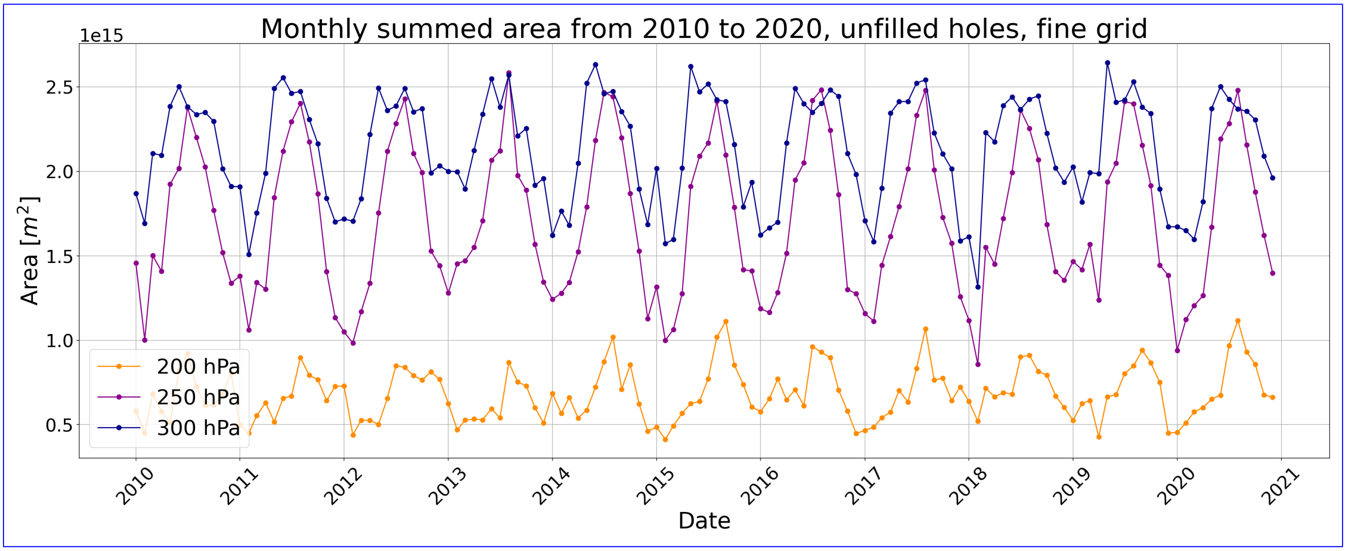

Figure 2. ISSR total area in each month from 2010 to 2020 at pressure levels of 200 hPa (orange), 250 hPa (violet) and 300 hPa (dark blue); here, the data in the ERA5 resolution is used, possible holes in the ISSRs are not filled.

total number of ISSRs. The cycle is most pronounced in the two lower levels ($p = 300\,\mathrm{hPa}$ and $p = 250\,\mathrm{hPa}$), while for the highest level ($p = 200\,\mathrm{hPa}$) the variation is weak but still apparent.

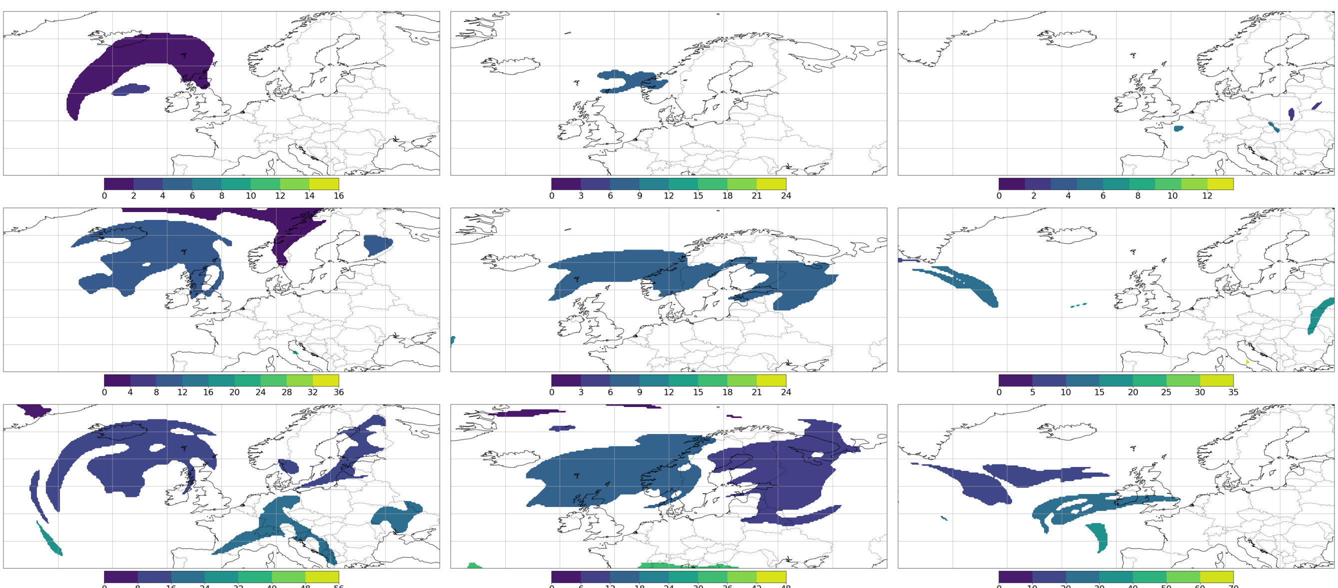

Figure 3. Exemplary ISSRs at pressure levels $p = 200\,\mathrm{hPa}$, $p = 250\,\mathrm{hPa}$, $p = 300\,\mathrm{hPa}$ (top to bottom) at three different times (3 columns) in January 2011. Colors are used to distinguish between individual ISSRs.

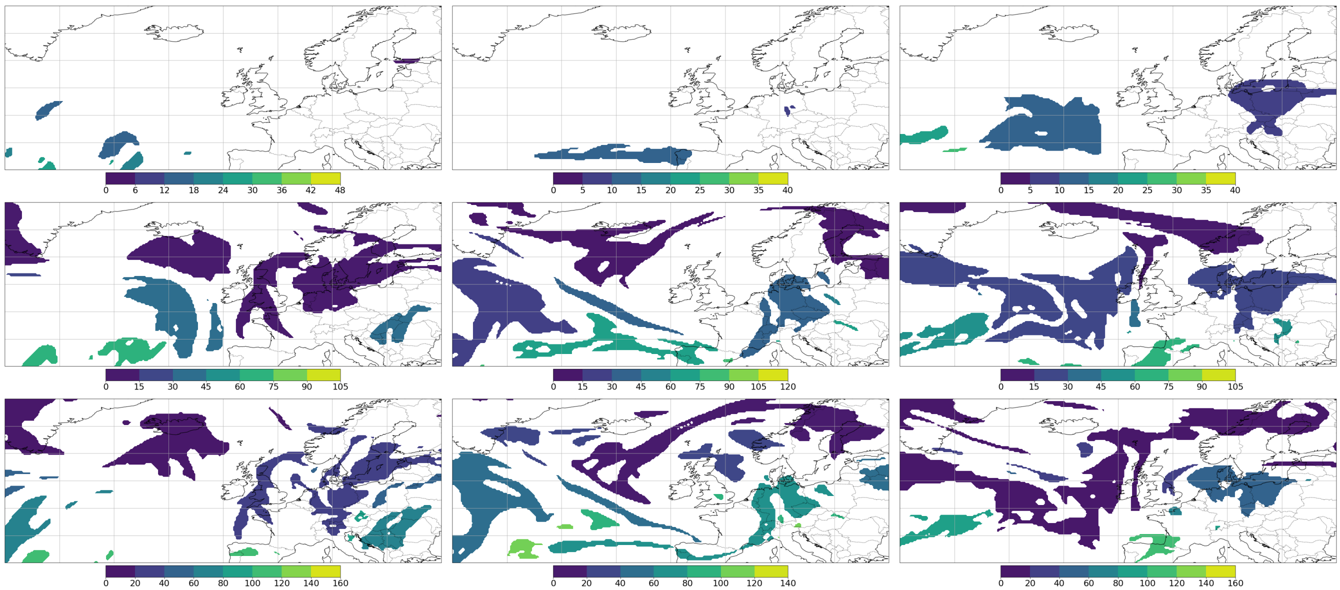

Figure 4. Exemplary ISSRs at pressure levels $p = 200\,\mathrm{hPa}$, $p = 250\,\mathrm{hPa}$, $p = 300\,\mathrm{hPa}$ (top to bottom) at three different times (3 columns) in July 2011. Colors are used to distinguish between individual ISSRs.

In Figure 3 ~~some~~ examples of ISSRs at the three different pressure levels over the North Atlantic region are presented for three times in January 2010, giving a snapshot. A similar example is shown in Figure 4 for one snapshot in July 2019 (3 times). ~~One can clearly see that in~~ In winter the ISSRs are discernibly more compact and ~~span only~~ cover a limited area (Fig. 3). At the highest altitudes (i.e. at pressure level ~~$p = 200hPa$~~$p = 200\,\mathrm{hPa}$) there are ~~no~~ very few ISSRs although at lower altitudes (higher pressures) ISSRs can be seen; in winter the tropopause is located at lower altitudes, thus the pressure level ~~$p = 200hPa$ is (probably~~$p = 200\,\mathrm{hPa}$ is (most likely) completely contained in the stratosphere. In contrast, in July we find ~~wide spread and quite~~ widespread and frayed ISSRs at all three pressure levels (Fig. 4). Even at ~~$p = 200hPa$~~ $p = 200\,\mathrm{hPa}$ ISSRs can be found, since during summer the tropopause is located at higher altitudes and ice supersaturation is present there.

The different shape of ISSRs in winter and summer, as observed in Figures 3 and 4, can ~~be also~~ also be seen in the (statistical) investigations of the fractal dimension, as described in the next section.

3.2 ISSR Dimension

~~We now determine~~ Next, the fractal dimension for all ISSRs in the data set ~~as~~ are derived using the methods explained in section 2.2. We calculate area and perimeter for each detected ISSR (i.e. each connected "island") and determine the fractal dimension by using all data of a certain pressure level for a whole month in a double logarithmic scatter plot. In Figure 5 an example ~~of this procedure~~ is shown for January ~~2020~~ 2017 (in appendix F another example is provided for July ~~2020~~2017). ~~Three different regimes can be determined in these scatter plots : (a) very small ISSRs with perimeters lower than $\sim 2 \cdot 10^5$m,~~

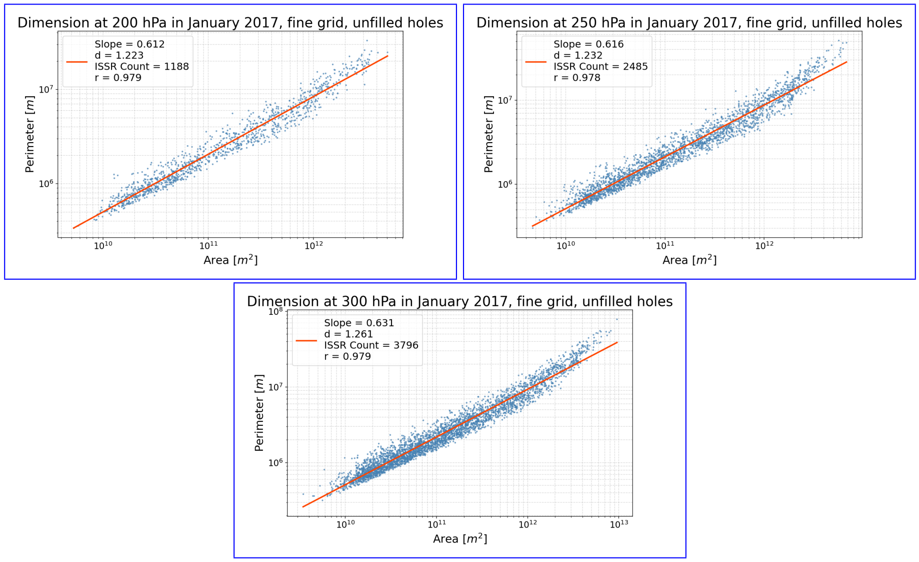

Figure 5. Determination of the fractal dimension via fits to the area-perimeter relation (eq. 4) in case of January 2017. Blue dots indicate the data points (tuple (A,P)), red lines are the fits from linear regression. Left: Pressure level $p = 200\,\mathrm{hPa}$; Middle: Pressure level $p = 250\,\mathrm{hPa}$; Right: Pressure level $p = 300\,\mathrm{hPa}$

~~(b) an intermediate regime containing most of the ISSRs (representing fractal characteristics), and (c) a regime of very large ISSRs with perimeters larger than $\sim 10^7\mathrm{m}$; for all three regimeswe see different signatures of fractal dimensions~~

In the scatter plots the data are confined to a linear point cloud. There is a perceptible scale break at perimeters of $P \sim 10^7\mathrm{m}$, separating two regimes. However, ~~the procedure of linear regression is applied to the intermediate regime, including most of the detected ISSRs. For this regime we obtain fractal dimension with values $\alpha \sim 1.55 - 1.70$.~~ this signature is weak, so we do not separate these two regimes in this evaluation. It might be related to the fact that the horizontal extension of objects on isobaric surfaces in the Earth's atmosphere is limited by the finite surface of the Earth. This can also be seen in the investigations of the horizontal extensions in Sec. 4.

~~The deviation from the regression line of ISSRs with very low perimeters (regime (a)) most probably represents single pixel ISSRs or ISSRs with very few pixels. The minimal amount of pixels limits the degree of irregularity and frayed boarders. Single pixels, which are approximated as rectangles, have dimension $\alpha = 2$ by definition. This steeper slope explains the appearance of the data points at low perimeters sufficiently well.In the intermediate regime (b), a linear relation is well pronounced with only small scatter around the linear regression line.~~ A linear regression is applied to the complete dataset of each respective month, and the resulting slope is used to determine the respective fractal or self-similar dimension, as indicated in Eq. (4). We find values in the range $D \sim 1.18 - 1.375$, i.e. values well above the value of $D = 1$ for a geometric object.

~~If we proceed to very large perimeters (regime (c)), there seems to be a kind of scale break at perimeters larger than $\sim 10^7\mathrm{m}$. For these very large ISSRs, we see a kind of bend in the scatter plot, indicating a smaller linear slope, thus implying a smaller fractal dimension.~~ As illustrated in the simple examples presented in appendix B, the reduction of fractal dimension for larger objects might be driven either by more elongated objects (as in case of the ~~ellipses pulled apart~~systematically stretched rectangular) or by more frayed objects. Both reasons seem to be plausible from the presented snapshots in Figs. 3 and 4; however, a clear attribution is not possible.

Finally, we determine the annual evolution of the fractal dimension ~~in regime (b)~~ as obtained from monthly data at different pressure levels; the results are represented in Figure 6. ~~First, we again~~ We see a clear separation by vertical levels. For each month, the fractal dimensions are ordered~~such that the highest value is~~ , with the smallest value assigned to pressure level ~~$p = 200$hPa~~$p = 200\,\mathrm{hPa}$, followed by the medium value at pressure level ~~$p = 250$hPa and the lowest~~ $p = 250\,\mathrm{hPa}$ and the highest value at pressure level ~~$p = 300$hPa, respectively~~$p = 300\,\mathrm{hPa}$. The fractal dimensions of the observed ISSRs are in the ranges ~~$\sim 1.61-1.69$ ($p = 200$hPa), $\sim 1.56-1.66$ ($p = 250$hPa~~$D \sim 1.18-1.29$ ($p = 200\,\mathrm{hPa}$), $D \sim 1.22-1.36$ ($p = 250\,\mathrm{hPa}$), and ~~$\sim 1.55-1.64$ ($p = 300$hPa), respectively~~$D \sim 1.26-1.375$ ($p = 300\,\mathrm{hPa}$). All fractal dimensions D show a strong seasonal cycle with ~~minima~~ maxima during summer and ~~maxima during winterseasons, respectively~~minima during winter. The amplitude for the cycles is largest for the pressure ~~range $p = 250$hPa, whereas it is reduced or damped for the other two levels~~level $p = 250\,\mathrm{hPa}$, followed by a slightly reduced amplitude for the pressure level $p = 300\,\mathrm{hPa}$; the variation of the monthly fractal dimension is smallest for the pressure level $p = 300\,\mathrm{hPa}$, but it is still well pronounced. The correlation coefficient for the linear fit ~~in the intermediate regime (b)~~ indicating the quality of the fits by the linear regression are ~~quite~~ relatively high ($r^2 \geq 0.95$). Thus, ~~the results are quite~~ we can conclude that these results are robust and constitute a new and pronounced feature of ISSRs. The influence of the grid resolution (i.e. grid coarsening) on the derived fractal dimension is discussed in Appendix C.

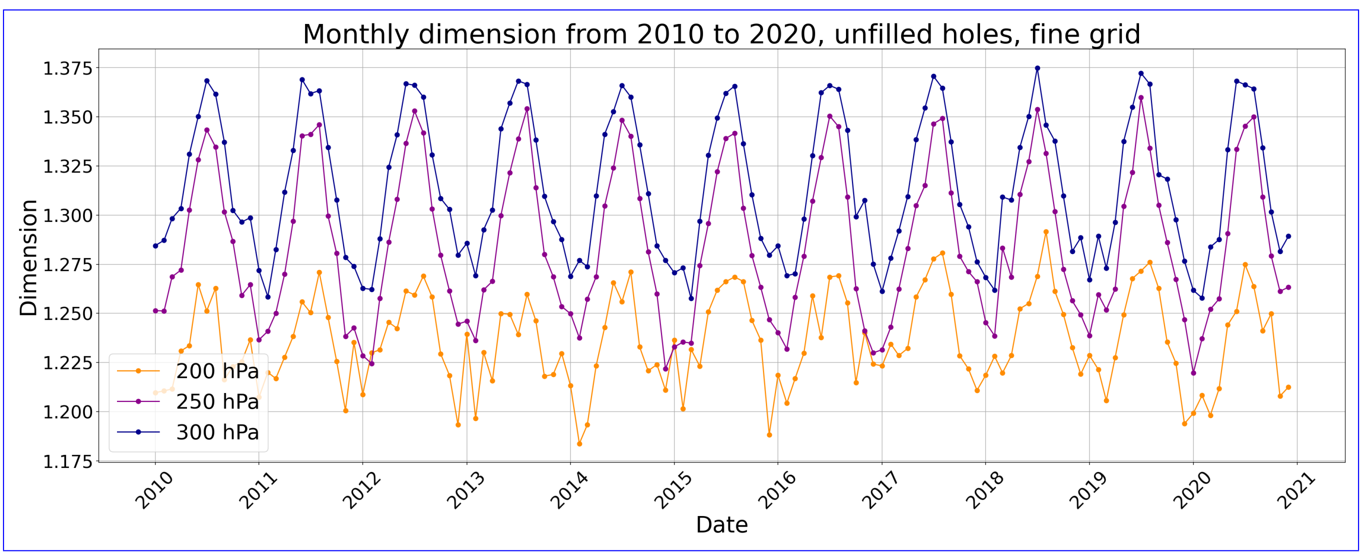

Figure 6. Fractal dimensions at three pressure levels (200 hPa in orange, 250 hPa in violet, and 300 hPa in dark blue) in a monthly resolution for the time span of 11 years of ERA5 data.

Although ~~, this study~~ this is the first ~~one~~ study investigating the fractal nature of ISSRs, we can try to compare our results to similar studies on fractal dimensions, e.g., for high clouds observed in satellite data and models with global storm resolving resolutions. Since ice clouds form in ISSRs, there should be a comparable relationship. Batista-Tomás et al. (2016) evaluated satellite data ~~of~~ (spacial resolution of 1 km) of (ice) clouds and found a fractal dimension of ~~$\alpha \sim 1.46$~~ $D = 1.37 \pm 0.02$ for high cirrus clouds, and a fractal dimension of ~~$\alpha \sim 1.70$~~ $D = 1.18 \pm 0.05$ for cumulonimbus clouds. These values are in the same range as values of ~~α~~ D found in this study, showing clear fractal properties of clouds. Christensen and Driver (2021) investigated satellite data (5 km grid) and high resolution model data (initialized using the ECMWF 9 km analysis, linear resolution of 2.5 to 7.8 km for the core ensemble) and found fractal dimensions in the range ~~$\alpha \sim 1.33 - 1.5$,~~ $D \sim 1.35 - 1.45$ for the satellite data, and $D \sim 1.27 - 1.53$ for the different (high-resolution) models, which are also comparable to our findings. ~~Note, that the values of the two studies are recalculated using our definition of fractal dimension in the perimeter-area relation in Eq. (4).~~ Since we are not distinguishing between cloudy and clear air inside ISSRs, there might be a mixture of different signatures of clouds and cloud free air massses (constituting all ISSRs). Nevertheless, these results show that ISSRs exhibit a clear signature of self-similarity.

3.3 Changes due to filled objects

In our investigations so far, we used the derived islands of ISSRs as we found them. Thus, these regions can have holes, as can be seen clearly in Figures 3 and 4. These holes increase the perimeter of the objects in our calculations, changing the fractal dimension, as discussed by Brinkhoff et al. (2015). This aspect can be seen from two different point of views.

1. We are investigating objects with an assumed self-similarity. As a consequence of this assumption we would expect the same structural properties on every scale, i.e. repeating the main features when we zoom into smaller scales. As known from theory there are objects like e.g. the Sierpinski triangle or the Sierpinski carpet (e.g., Florio et al., 2019) with holes, leading to the general structure of the object, and also to the respective fractal dimension. For clouds as macroscopic objects on different scales, we might assume a similar property. If we zoom into a smaller scale, we still find some holes in the cloudy object, thus we could assume that the "holes" inside the ISSRs should be an important feature. A similar feature can be seen in case of high resolution measurements of water vapor, leading to pathlengths of ISSRs on a much smaller scale (see discussion in Spichtinger and Leschner, 2016, their section 5). From this point of view, the use of unfilled ISSRs would be meaningful, or even mandatory, since their structure with holes is a key feature.

2. Following the discussion by Brinkhoff et al. (2015), holes in the observed objects (clouds, ISSRs, etc.) might artificially result from the detection procedure. Since it is not really clear which features are real and which are of artificial nature, it is more meaningful to fill the holes and to evaluate the filled objects. This procedure was suggested by Brinkhoff et al. (2015) and was also applied by Christensen and Driver (2021).

These two aspects are, of course, relevant for our investigation. So far, we have used the first approach, using the ISSRs as they are, assuming that the holes are relevant for the inherent structure of these objects. However, for investigating the impact of a possible erroneous description of islands, we repeat the evaluation of the whole data set again using a filling of occurring holes in the islands rather that eliminating the objects with holes.

In Figure 7 we show the results of the monthly timeseries of fractal dimension on the three pressure levels.

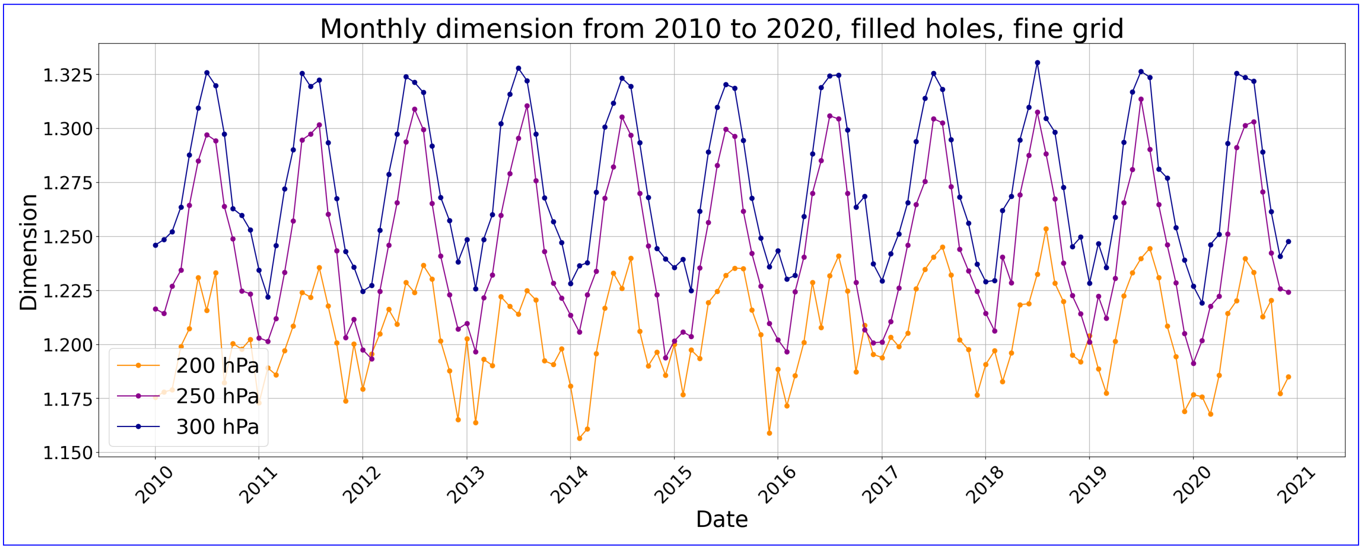

Figure 7. Fractal dimensions at three pressure levels (200 hPa in orange, 250 hPa in violet, and 300 hPa in dark blue) in a monthly resolution for the time span of 11 years of ERA5 data; the possibly occurring holes in the ISSRs islands are filled.

We find that the qualitative behavior of the monthly derived fractal dimension remains the same, even for the filled ISSRs. We still see the vertical layering of the dimension at different pressure levels with the same seasonal cycle as the unfilled ISSRs. However, there is, as expected, a change in the values of the fractal dimensions. The values of D for filled objects are reduced by an absolute value of about $\Delta D \sim 0.03 - 0.05$, with smallest deviations for the pressure level $p = 200\,\mathrm{hPa}$ and largest deviations for the pressure level $p = 300\,\mathrm{hPa}$. Nonetheless, the filled objects show the feature of a self-similarity with dimensions $D > 1$.

Finally, we want to remark that for the upcoming evaluation of the ISSRs in terms of horizontal extensions or pathlengths (see section 4), we will stay with the unfilled ISSRs, since the local structure is more relevant for these investigations.

4 Horizontal ~~span~~ extension of ISSRs

Although ISSRs are quasi 2D objects on isobaric surfaces, a common measure for ISSRs is the so-called pathlength. If a (commercial) aircraft crosses an ISSR, the track inside the ISSR is termed as pathlength. Gierens and Spichtinger (2000) first investigated pathlength statistics of ISSRs using data from the MOZAIC project (Marenco et al., 1998), this study was later extended by Spichtinger and Leschner (2016) for ~~IAGOS data~~ the IAGOS data set (Petzold et al., 2015). The pathlengths, although constituting just 1D tracks through 3D objects, give a first idea about the horizontal extension and even the shape of

ISSRs. Since we use quasi 2D data (at pressure levels) in this study, we can generate artificial pathlengths in order to simulate the distribution of realistic pathlengths. These can be used in two different ways. First, using zonal and meridional directions (i.e. East-West, North-South, respectively), we can statistically investigate the horizontal extension (or span) of ISSRs in a systematic but less realistic way~~(if one thinks about flight tracks)~~. Second, we can generate realistic pathlengths in using simulated flight tracks along geodesics between frequently used airports. These pathlengths then can be compared to ~~realistic~~ distributions as derived from aircraft data ~~(e.g. from the IAGOS project, see Petzold et al., 2015)~~(e.g. from the IAGOS project Petzold et al
.

For the determination of longitudinal and latitudinal extensions or spans of ISSRs, we proceed as follows. These spans are not measured as a means to obtain the largest extent in one direction, but rather to generate a full set of spans along latitudes/longitudes touched by the respective ISSR. Thus, the ISSR is therefore measured in "slices" with a spacing of 0.25 degrees. This procedure is carried out for both directions, zonal and meridional, respectively. The resulting data is divided by seasons, i.e. ~~spring (MAM),~~ summer (JJA) ~~, autumn (SON)~~ and winter (DJF), and is used for deriving statistical distributions of the horizontal extension/spans of ISSRs. Note that we use the "unfilled" ISSRs as a basis for the evaluation, since we are interested in the real distances of ISSRs; filling the holes of ISSRs would lead to artificially enhanced pathlengths. Since one application of this evaluation could be the issue of avoiding ISSRs for reducing the non-CO_2 effects of aviation (i.e. contrails, Petzold et al., 2025), the real horizontal extension of ISSRs including interruptions inside the ISSR are of importance. We report the mean and median values for the filled ISSRs in the respective tables.

Former investigations of pathlength statistics showed Weibull-type distributions (Gierens and Spichtinger, 2000; Spichtinger and Leschner, 2016)~~. ISSRs are extreme events in some sense, since the majority of data points in the ERA5 data set (and even in other data sets) show values below ice saturation. Just a small amount of regions in the UTLS are in the status of ice supersaturation. The~~ , or at least the distributions could be well represented using Weibull-type fits. However, we emphasize that the application of the Weibull distribution in this context is purely empirical. In contrast to classical extreme-value statistics, we do not consider maxima of underlying distributions, but rather the full population of pathlengths. Therefore, a strict interpretation in the framework of extreme-value theory is not appropriate here. Instead, the Weibull distribution is ~~one special case of the more general extreme value distribution (see, e.g., Sornette, 2006), thus it is not that surprising to find this type of distributionsin our investigation of "extreme events" ISSRs.~~ used as an empirical fitting function that provides a good representation of the observed distributions and allows for a compact characterization via its parameters, which is consistent with above mentioned studies studying ISSR distributions.

The probability density function of a Weibull distributed random variable x is given by $f(x) = \gamma p x^{p-1} \exp(-\gamma x^p)$ with shape parameter $p \in \mathbb{R}_+$ and scale parameter ~~$\gamma \in \mathbb{R}$, respectively~~$\gamma \in \mathbb{R}_+$. The parameter p determines the overall shape of the distribution; it can be obtained by using a Weibull plot (and the cumulative distribution $F(x) = 1 - \exp(-\gamma x^p)$) with linear regression. The slope of the regression line is the parameter p. For more details about Weibull plots we refer to appendix E.

4.1 Span along Longitude

First, we investigate the ~~latitudinal~~ longitudinal slices, i.e. pathlengths along longitudes in North-South direction. ~~The~~ Since the major variation of horizontal extensions is between winter and summer, we exclusively show these distributions in all respective figures. The mean values for all four seasons are then reported in the respective Tables. The normalized statistical distributions for ~~the four seasons~~winter and summer, differentiated into three pressure levels are shown in Figure 8. Here, we use the full data set for the ~~whole~~ period between 2010 and ~~2020.~~ 2020 using the data with unfilled holes. The corresponding figures based on the data set with filled holes are provided in Appendix G, the mean and median values are reported in table 1.

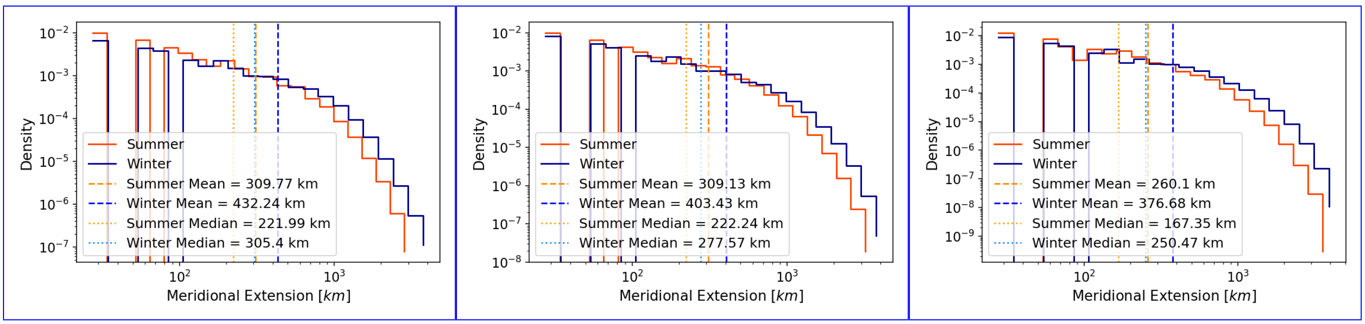

Figure 8. Distributions of meridional span (i.e. pathlengths in North-South direction) for summer (JJA, orange colors) and winter (DJF, blue colors) using data with unfilled holes. Mean values are indicated by vertical dashed lines, median values are indicated by vertical dotted lines. Left: 200 hPa, Middle: 250 hPa, Right: 300 hPa

For ~~the pressure pevels $p = 250/300$hPa~~all pressure levels $p = 200/250/300\,$hPa, the mean North-South span of ISSRs is significantly higher in winter as compared to the summer months~~, while autumn and spring exhibit minimal disparity. For the lowest pressure level (i.e. highest altitude, $p = 200$hPa), we find a slightly different behavior, i.e. the maximum mean value occurs for spring season, whereas the minimum remains in summer.~~ . While the density does not differ much between the seasons for ISSRs up to a size of approximately ~~10^6 m~~10^3km, the disparity between summer and winter gets larger with increasing the measured span. The absolute mean span increases with decreasing pressure (i.e. with rising altitude levels); the relative difference comparing summer and winter ~~also~~ slightly increases with higher pressure (i.e. lower altitudes). ~~The mean~~ All values are reported in Table ~~??~~1. The strong seasonal cycle is present in both, the mean values and also in the extreme tails of the distributions. For winter, the season with maximum mean values~~(winter for $p = 250/300$hPa, spring for $p = 200$hPa), we find an clearly~~ , a clear enhanced probability of finding extremely large pathlengths (i.e. enhanced values in the tail of the distribution) can be seen, whereas during summer there is a reduced probability of extremely large pathlengths. The histograms are not symmetric but right-skewed, so the mean is pulled upward by few large ISSRs. The median is more robust and thus more suitable to assess the typical 2D features of ISSRs. The median behaves similarly to the mean in that it generally decreases with increasing pressure. The exception being a minor increase from 200 hPa to 250 hPa in the summer months. This behaviour is not observable in winter. As the distribution presents right-skewed, the median is significantly smaller than the mean across pressure levels and seasons, thus the few large events in the tail of the distribution shift the mean towards larger values. This suggests possibly two regimes and/or formation mechanisms (e.g., synoptic-scale vs localized), which is discussed later in more details.

All histograms show bars representing ~~single pixel and very~~ small ISSRs. The distributions have a strong similarity to Weibull distributions as found in former investigations (e.g. Gierens and Spichtinger, 2000; Spichtinger and Leschner, 2016). Therefore, we use Weibull plots (~~Figure ??~~see Figure 9) for further evaluations, i.e. to determine the approximate shape parameter of the distribution.

The data used deliberately does not include measurements shorter than ~~27km~~27 km, as this is approximately the longest single-pixel length that can be measured in the target region. Including distances below that threshold is not meaningful, since this would introduce artificial biases stemming from different pixel sizes at different locations, leading to artificial breaks of regimes. Note, that we still use the data set with the restriction of a minimum of 24 pixels per ISSR. This might also crucially reduce the number of small ISSRs in the evaluation.

The data shows two regimes with roughly linear correlation but different slopes in the Weibull plots (i.e. in the respective values of parameter p). Thus, there are two distinct distributions superimposed in the histograms. The transition between these regimes is roughly located at ~~$\sim 10^5$ m~~ $\sim 2\cdot 10^2$ km; for the smaller ISSRs we find values of $p\sim 1.5$, whereas for the larger ISSRs the distribution is close to an exponential distribution $p\sim 1$. This alludes to the existences of two different physical formation processes. Neither season nor pressure level influences this observation.

The ~~existence~~ presence of two clearly separated ~~regions in size points to possibly~~ size regimes suggest potentially different formation mechanisms of ISSRs ~~on different~~ operating at distinct spatial scales, i.e. processes acting on distinct but different scales, ~~producing a distinct scale in the horizontal extension of ISSRs~~leading to characteristic horizontal extents. However, this hypothesis is subject of further investigations, since an in depth analysis is out of scope of this study.

~~The number of points for the 'small regime' is quite small, we only use a linear fit for the regime or larger ISSRs. Here, we can derive the shape parameter p as the slope of the linear fit. We find almost no variation in the shape parameter p, but values in the range $p\sim 1.01-1.06$.~~

	Filled holes				Unfilled holes			
	Mean		Median		Mean		Median	
	DJF	~~MAM~~ JJA	DJF	JJA	~~SON~~ DJF	JJA	DJF	JJA
200 hPa	~~222.90~~ 459.59	~~250.42~~ 329.10	~~184.90~~ 306.54	~~203.31~~ 222.26	432.24	309.77	305.40	221.99
250 hPa	~~280.81~~ 434.37	~~234.33~~ 339.14	~~161.09~~ 278.45	~~210.98~~ 222.85	403.43	309.13	277.57	222.24
300 hPa	~~273.89~~ 410.97	~~215.79~~ 283.72	~~158.59~~ 251.14	~~214.42~~ 194.48	376.68	260.10	250.47	167.35

Table 1. Mean and median values of ~~latitudinal~~ the meridional span (~~i.e. pathlengths~~ pathlength in ~~North-South~~ north–south direction~~)~~ ~~statistics (~~, in km) for DJF and JJA at different pressure levels, for ISSRs with filled and unfilled holes.

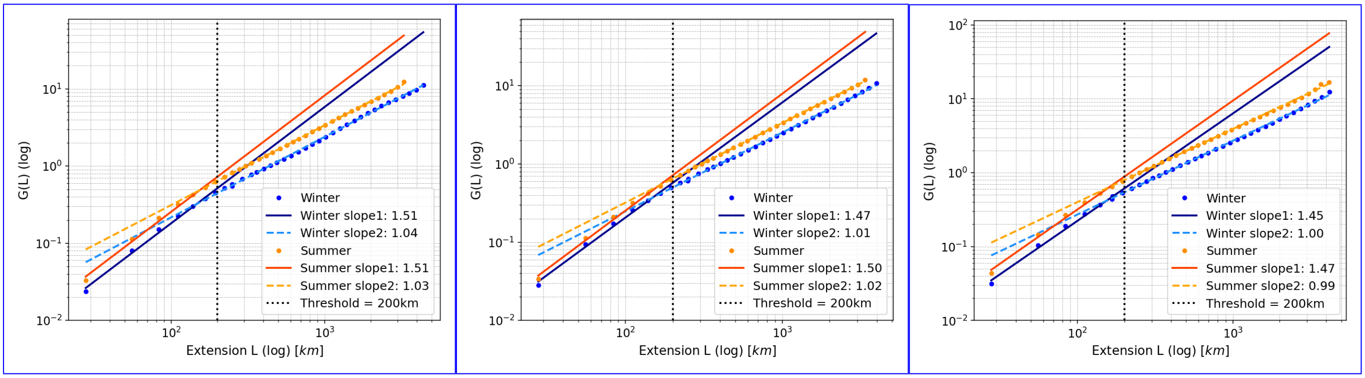

Figure 9. Weibull plots for the pathlength distributions in North-South direction using data with unfilled holes. The linear regression fit is shown for the regimes of pathlengths smaller and larger than $\sim 2 \cdot 10^2\mathrm{km}$ (dashed vertical line). Blue/orange colors indicate winter/summer data, respectively. The fits to the different regimes are represented by a dashed and a solid line. Left: $200\,\mathrm{hPa}$, Middle: $250\,\mathrm{hPa}$, Right: $300\,\mathrm{hPa}$

4.2 Span along Latitude

Alike investigating the North-South slices along longitudes, we now investigate horizontal extensiosn or spans along latitudes, i.e. slices in East-West direction within ISSRs. The normalized statistical distributions for the ~~four seasons~~ two seasons (summer/winter), differentiated into three pressure levels are shown in Figure ~~??~~10. Again, we use the full data set for the ~~whole~~ period between 2010 and 2020.

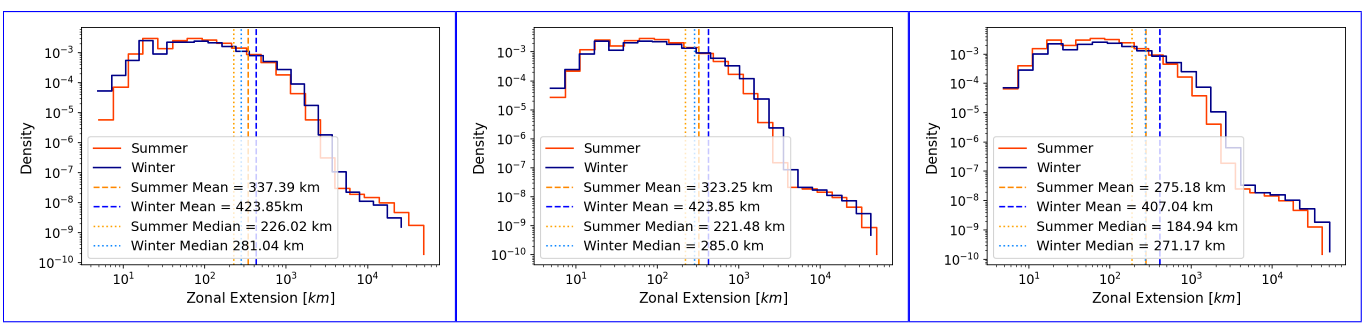

Figure 10. Distributions of zonal span (i.e. pathlengths in East-West direction) for different seasons, i.e. summer (JJA, orange colors) and winter (DJF, blue colors), using data with unfilled holes. Mean values are indicated by vertical dashed lines, median values are indicated by vertical dotted lines. Left: $200\,\mathrm{hPa}$, Middle: $250\,\mathrm{hPa}$, Right: $300\,\mathrm{hPa}$

The distribution of measured latitudinal distances shows almost the same qualitative characteristics as the longitudinal counterpart. We see a strong decrease in frequency of occurrence for spans larger than the mean values. However, in contrast to the longitudinal distributions, there is an additional very small mode at very large spans ($\sim 10,000\,\mathrm{km}$), indicating the occurrence of very few very large ISSRs in East-West direction. For all pressure levels, the mean span is significantly higher in the winter months compared to the summer months. ~~Spring and autumn showcase distances between the summer and winter mean and differ only slightly from another.~~ Differences in the distribution of spans by season are most clear for larger spans. The mean generally decreases slightly with a higher pressure level~~, with only the exception of the autumn mean being higher at $p = 250$hPa compared to the level at $p = 200$hPa~~. The decrease in mean span with higher pressure is ~~most~~ more evident in the summer months. Analogous to the meridional observations, the median is consistently lower than the mean. The median increases slightly from 200 hPa to 250 hPa with the exception of summer using unfilled data. It is lowest at the highest pressure level. As with the meridional span, this right-skewed distribution strengthens the case for using Weibull distributions to further investigate the extensions. ~~The mean~~All values are reported in Table ~~??~~2, together with the mean/median values for the filled ISSRs. We also see the same feature of enhanced probability for extremely large pathlengths during winter and reduced probability during summer~~, respectively.~~

. ~~We again~~

In Figure 11 we investigate the Weibull plots for the distributions. For the East-West spans~~it seems that here are three different regimes . A~~, three distinct regimes appear to be present. There is a regime of very small ~~pathlengths with no~~ latitudinal spans (up to $\sim 10^2$, km), without a clear Weibull signature ~~, and the two regimes with almost constant but different parameter p as before~~in the Weibull plot. In addition, there are two further regimes, separated at values ~~$\sim 10^5$m. The two distinct (Weibull) regimes are more distinguishable compared to the latitudinal data.~~ $\sim 2 \cdot 10^3$ km, which clearly show linear behavior in the Weibull plots, thus indicating two different regimes and clearly distinguishable by a different Weibull parameter p. The regime of intermediate spans of ISSRs results into an almost exponential distribution (Weibull parameter $p \sim 1$), whereas the regime of very large spans clearly show a Weibull charactersistics with parameter $p \sim 0.2$; this characteristics remains almost the same over the seasons.

The regime of very small ~~pathlength~~ pathlengths might be an artifact of the evaluation. The real area of a pixel (or grid point) depends crucially on the latitude. For East-West spans we regularly scan through at all latitude, thus high latitude circles will systematically produce small horizontal sizes for ISSRs consisting of few pixels.

	Filled holes				Unfilled holes			
	Mean		Median		Mean		Median	
	DJF	~~MAM~~ JJA	DJF	JJA	~~SON~~ DJF	JJA	DJF	JJA
200 hPa	~~417.72~~ 450.53	~~382.09~~ 359.24	~~333.90~~ 286.64	~~374.60~~ 230.91	423.85	337.39	281.04	226.02
250 hPa	~~414.48~~ 457.94	~~374.45~~ 354.74	~~318.12~~ 298.21	~~384.74~~ 232.38	423.85	323.25	285.00	221.48
300 hPa	~~397.04~~ 445.54	~~343.80~~ 299.69	~~270.71~~ 285.22	~~351.53~~ 192.78	407.04	275.18	271.17	184.94

Table 2. Mean and median values of ~~longitudinal~~ the zonal span (~~i.e. pathlengths~~ pathlength in ~~East-West~~ east–west direction~~) span statistics (~~, in km) for DJF and JJA at different pressure levels, for ISSRs with filled and unfilled holes.

~~We derive the shape parameter only for the regime with pathlengths larger than 10^5m. The parameter values only slightly vary, with values $p \sim 1.02-1.07$~~The tiny mode of very large spans of ISSRs up to few ten thousands of kilometers might indicate the impact of synoptic and large scale weather systems, triggering atmospheric flows in the zonal direction with a persistent vertical upward motion, thus leading to a persistence of ice supersaturation in the UTLS. The upper bound of such synoptically driven ISSRs is, of course, given by the circumference of the Earth at certain latitudes.

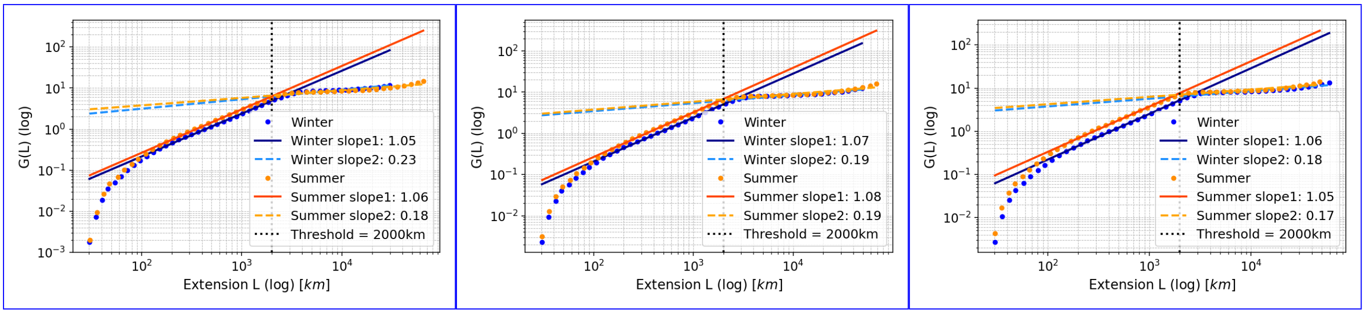

Figure 11. Weibull plots for the pathlength distributions in East-West direction using data with unfilled holes. The linear regression fit is shown for the regimes of pathlengths smaller and larger than $\sim 2 \cdot 10^3$km (dashed vertical line). with a clear scale break at $\sim 2 \cdot 10^3$ km (indicated by a dotted line). Blue/orange colors indicate winter/summer data. The fits to the different regimes are represented by a dashed and a solid line. Left: 200 hPa, Middle: 250 hPa, Right: 300 hPa

4.3 Span along modeled aircraft tracks (pathlengths)

In addition to the rather artificial longitudinal and latitudinal measurements, realistic pathlengths are investigated. In lieu of real in situ measurements, some tracks of commercial aircraft routes are investigated. For this purpose we exemplarily chose four typical flight routes between the US and Europe, based on the flight tracks frequently found in the IAGOS data (Petzold et al., 2015). The ~~four~~ three tracks, i.e. direct flight routes are Berlin–Chicago, Frankfurt–Atlanta, ~~London–New York,~~ and Paris–Miami, ~~respectively,~~ placed on the geodesics on a sphere (~~see~~ Figure 12). The pathlengths are obtained by measuring the distance along the sections of ice supersaturation on the flight track from airport to airport. The histograms (Figure 13) show numerical artifacts for small ~~and single pixel~~ ISSRs. However, we find the same features of pathlength statistics for mean values and distributions as ~~before.With the exception of spring at $p = 200$hPa, the~~ in Secs. 4.1 and 4.2. The winter months yield the highest mean pathlengths ~~, followed by spring and autumn with similar length and summer with~~ while summer brings forth the shortest mean distances. ~~The mean summer pathlength is shorter the higher the pressure. This is only true for the other seasons when comparing values at $p = 250$hPa to those at $p = 300$hPa. The difference in probability is more apparent for larger distances.~~ For all seasons there is an increase of mean and median values with increasing heights: The highest mean/median pathlengths can be found at the highest level ($p = 200$ hPa), and the lowest values at $p = 300$ hPa with intermediate values at the level $p = 250$ hPa. The distributions mostly agree for the two seasons, with a larger deviation for the largest pathlengths, explaining also the seasonal difference. During winter, there are more large ISSRs than during summer. The mean values of the pathlength distributions are represented in ~~table ??~~Table 3.

In the evaluation of the Weibull plots (Fig. 14), we find ~~again~~ two different regimes of distinct Weibull distributions with different values of p, separated at pathlengths ~~$\sim 10^5$m, as before~~$\sim 10^2$ km, as for the longitudinal extensions (North-South). However, the difference in the regimes is more pronounced than in the former ~~evaluations of North-South and~~ evaluation, and the clear signal of the very large zonal extensions (East-West ~~extensions. For the large pathlength regime we see a more pronounced seasonal cycle, as clearly represented in the values of Weibull parameter p, thus resulting into distinct changes in the tail of pathlength distribution. For winter season, we find more large pathlengths (i.e. higher values $p \sim 1.07 - 1.112$)~~direction) is missing in this evaluation. As before, we skip the very small pathlengths in the linear regression, since the probabilities are probably biased by the selection process (leaving out regions smaller than 24 pixels). For both regimes, the seasonal cycle is

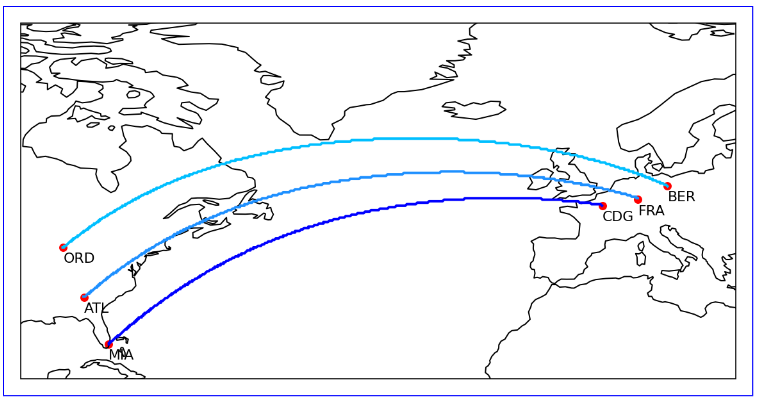

Figure 12. Typical flight routes of commercial air traffic for some important airports in the US (Chicago, Atlanta, Miami) and Europe (Berlin, Frankfurt, Paris). These flight routes can be seen in the measurement data from the IAGOS project.

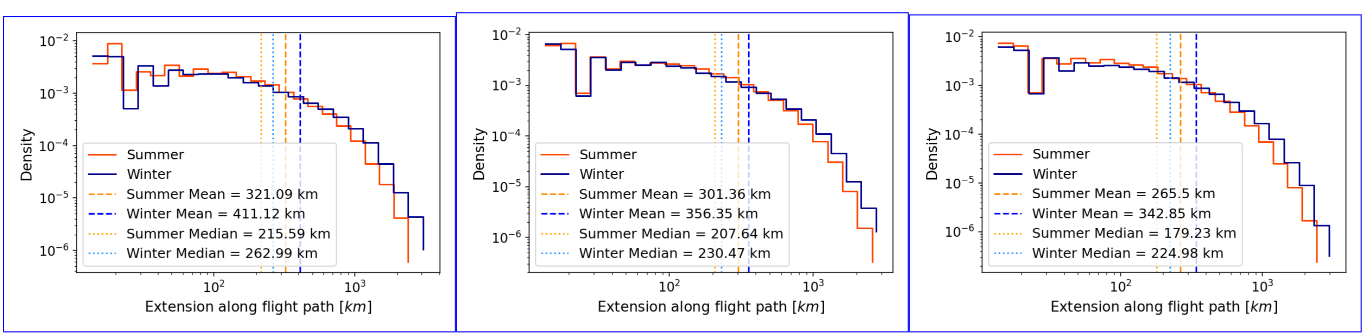

Figure 13. Distributions of realistic pathlengths for different seasons as simulated by assuming common flight tracks (as shown in fig. 12) using data with unfilled holes for different seasons, i.e. summer (JJA, orange colors) and winter (DJF, blue colors), using data with unfilled holes. Mean values are indicated by vertical dashed lines, median values are indicated by vertical dotted lines. Left: 200 hPa, Middle: 250 hPa, Right: 300 hPa

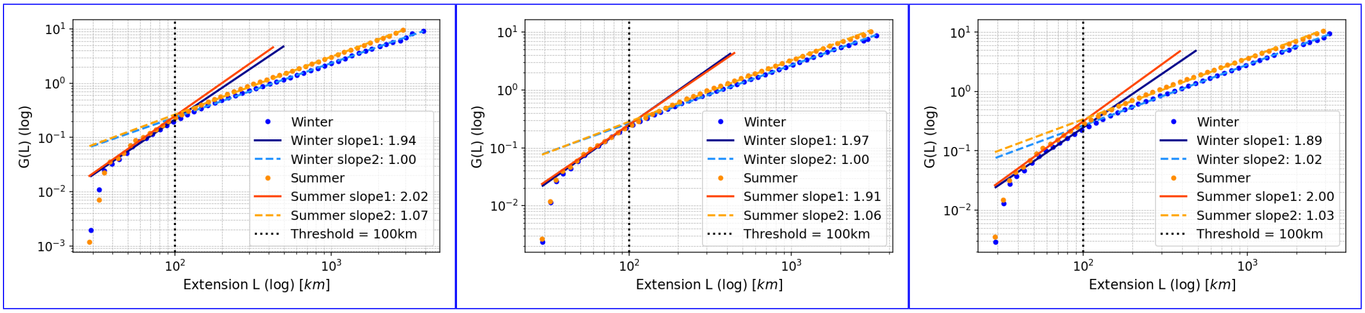

Figure 14. Weibull plots for the pathlength distributions of realistic pathlengths simulated by common flight tracks using data with unfilled holes. The linear regression fit is shown for the regimes of pathlengths between 40 km and $\sim 10^2$km and pathlengths larger than $\sim 10^2$km, this threshold being indicated by a dotted line. Blue/orange colors indicate winter/summer data, respectively. The fits to the different regimes are represented by a dashed and a solid line. Left: 200 hPa, Middle: 250 hPa, Right: 300 hPa

not strongly pronounced. In the small pathlengths regime, we find values $p \sim 1.95$, whereas in ~~summer less large pathlengths can be found ($p \sim 0.91 - 0.95$).~~ the regime of large pathlengths, the values are close to an exponential distribution, i.e. $p \sim 1$. This signal is very robust, with almost no seasonal variation in the parameters or with respect to the different levels.

~~The mean values as well as the distributions for the artificial pathlengths as obtained from the ERA5 data agree very well with evaluations of pathlengths using IAGOS data (Spichtinger and Leschner, 2016). The distribution also are of Weibull type, however with a clearer scale break and thus well separated regimes. Using a coarsening of the high resolution aircraft data, the mean values are in the same range as in our investigation (mean values $\sim 220 - 280$km).~~

4.4 Agreement of pathlength distributions

The results of the longitudinal, latitudinal and pathlength measurements agree well with another. The observation of the summer months yielding the shortest and ~~(mostly)~~ winter the longest mean distances generally holds true across methods.

	~~DJF~~ Unfilled holes ~~MAM~~ Mean		Median	
	DJF	JJA	~~SON~~ DJF	JJA
200 hPa	~~204.33~~ 411.12	~~229.36~~ 321.09	~~166.18~~ 262.99	~~185.09~~ 215.59
250 hPa	~~256.93~~ 356.35	~~213.59~~ 301.36	~~144.73~~ 230.47	~~191.97~~ 207.64
300 hPa	~~251.93~~ 342.85	~~196.64~~ 265.50	~~141.59~~ 224.98	~~194.79~~ 179.23

Table 3. Mean and median values of ~~pathlength~~ pathlengths (i.e. artificial flight tracks~~) statistics (~~, in km) for DJF and JJA at different pressure levels, based on ISSRs with unfilled holes.

This agreement applies to most results in terms of dependence on pressure level as well. The mean span is generally larger at lower pressures, i.e. higher up in the atmosphere~~.~~

~~The results of the simulated IAGOS flights in winter not completely following this pattern can be explained by both, the smaller amount of measurements compared to observing the whole atmosphere, and the tropopause being below 200 hPa in winter and thus skewing the results. The similarity of the results for latitudinal and longitudinal span speaks for the invariance of shape to zonal and meridional alignment.The~~ ; while this is always true for the comparison between levels $p = 200\,\mathrm{hPa}$ and $p = 300\,\mathrm{hPa}$, in the intermediate level $p = 250\,\mathrm{hPa}$ some variations can be seen. The mean values for East-West spans are generally larger than for the North-South extensions and the flight track pathlengths. ~~THis~~ This feature is obvious from the example of ISSRs as ~~show in figs.~~shown in Figs. 3 and 4. The ISSRs usually extend more in East-West direction, as driven by the mean large scale flow. ~~Finally~~

The results of the simulated IAGOS flights have a larger qualitative agreement with the meridional extensions. In both cases, there is ~~agreement in terms of the scale break in the distributions, manifested in the Weibull plots, which point to two possible physical processes forming ISSRs yielding two distributions.~~ a scale break at $L \sim 10^2\,\mathrm{km}$, separating two different modes of Weibull distributions. The tiny mode of exceptionally large spans as found in the zonal slices cannot be detected in the pathlengths of realistic flight tracks, since these very few, very large ISSRs are mostly elongated into zonal direction. Usual flight pattern along geodesics must certainly cross them for reaching the respective destination.

5 ~~Discussion~~

~~As described in the sections above , we found several properties of ISSRs in terms of fractal dimensions and horizontal extensions. More precisely, we~~ As we investigate ISSRs on fixed pressure levels. Thus, the seasonal variation of the tropopause, which is closely correlated with ice supersaturation (Spichtinger et al., 2003a), might result into fewer ISSRs during winter time at high altitude levels and skew the results.

The distributions as well as the mean (and median) values of the simulated pathlengths compare qualitatively well with the former investigations of pathlengths as obtained from aircraft measurements (Gierens and Spichtinger, 2000; Spichtinger and Leschner, 20 . The mean (and median) values as obtained from the ERA5 data are generally larger than in case of aircraft data. This is not surprising, since the aircraft data has a much higher temporal (and thus spatial) resolution; even for running means over the data set, mimicking a coarser resolution, the data still has a signature of small scale events. The Weibull shaped distributions can be seen in all evaluations, with a more or less prominent feature of a scale break at pathlengths $L \sim 10^2\,\mathrm{km}$. However, the fitted Weibull parameter of the distributions differ between aircraft data and ERA5 evaluation, although the general feature of a smaller slope for pathlengths below the scale break and a higher slope for pathlengths above the scale break is present in all evaluations. The difference in slopes for aircraft vs. ERA5 data is likely due to the different resolutions of the data sets. Finally, we see that the range of the obtained distributions of pathlengths is roughly the same in all investigations (ranging from few $10\,\mathrm{km}$ up to $\sim 5000\,\mathrm{km}$).

5 Conclusion, Discussion and Outlook

5.1 Conclusion

Ice supersaturated regions in the UTLS are important potential formation regions of ice clouds and contrails. For a better understanding of these regions and thus a meaningful representation in models on different scales and resolutions, we investigated ISSRs in ERA5 data as "macroscopic" and quasi two dimensional objects on pressure levels in the UTLS. We can summarize the main findings as follows:

1. The analysis of the area–perimeter relationship demonstrates that ISSRs in the UTLS exhibit self-similar (fractal) behavior, with dimension values between 1 and 2, as expected for planar structures with irregular boundaries. Pathlength statistics are consistent with these fractal properties.

2. There is a seasonal cycle in the number of ISSRs. We find many ISSRs for the summer season, ~~but~~ much less in winter. There is also a vertical layering of the amount of ISSRs, with high numbers at lower altitudes, and a decrease in the number for increasing heights.

3. ~~We find two main different regimes for the fractal dimensions in the parameter space of perimeter vs. area. For an intermediate regime with perimeters not larger than~~ $\cancel{\sim 10^7\mathrm{m}}$~~, we find fractal dimensions in order of~~ $\cancel{\alpha \sim 1.55 - 1.7}$~~; for the larger regime we find a even smaller values of the fractal dimension~~For the area of ISSRs we find the same type of seasonal cycle with high values during summer and low values during winter. The vertical layering is the same for the total number of ISSRs.

4. For the fractal dimension of ISSRs we find values in the range $1.175 \leq D \leq 1.375$. The fractal dimensions also show a ~~clear~~ distinct vertical layering with largest values for high altitudes and lower values for low altitudes~~, respectively.~~. For filled ISSRs the fractal dimension is systematically lowered by about $\Delta D \sim 0.02 - 0.05$, however still showing a fractal characteristics of $D > 1$.

5. There is a clear seasonal cycle for the fractal dimensions with smaller values for summer and larger values for winter~~, respectively.~~. This signal appears on all considered pressure levels.

6. In the evaluation of the horizontal extensions of ISSRs, i.e. deriving ~~pathlength~~ pathlengths in various ways (artificial East-West and North-South spans vs. realistic flight paths), we ~~also~~ find a seasonal cycle as well. Generally, we find smaller pathlengths during summer (smaller mean values, less extremes), whereas during winter the pathlengths are generally larger (larger mean value, more really large pathlengths). This feature is robust for all evaluated pressure levels.

7. In the realistic pathlengths statistics, we find different regimes, as also indicated by different values of the shape parameter p in the Weibull plots, indicating a superposition of two different Weibull distributions. The scale break can be estimated at $\cancel{L \sim 10^5\mathrm{m}}$ $L \sim 2 \cdot 10^2\mathrm{km}$, which is comparable to former investigations.

~~As we have see from~~

5.2 Discussion

As can be seen in the simple exercise in appendix B about changes in fractal dimensions, more elongated or even strongly frayed objects have ~~smaller fractal dimensions~~ larger fractal dimensions than their strictly geometric counterparts (i.e. $D > 1$). As indicated by the snapshots in Figs. 3 and 4, in summer the ISSRs ~~might be~~ are more elongated and ~~certainly~~ more frayed than in winter. The fractal dimension is ~~smaller~~ larger for ISSRs in summer, thus we expect more frayed/elongated objects. In turn, these objects ~~lead to smaller pathlengths, since crossing such objects lead to generally~~ result in shorter pathlengths, as traversing them generally involves smaller cross sections of ice supersaturation. On the other hand, ISSRs in winter have ~~larger~~ smaller fractal dimensions, thus suggesting a more compact shape. This is consistent with the pathlength statistics, ~~since crossing of~~ as traversing more compact objects ~~leads to less small pathlengths or even to generally~~ results in fewer short pathlengths and, on average, larger cross sections. Thus, the seasonal cycles of fractal dimensions and pathlengths ~~, respectively,~~ are physically consistent.

The strong contrast between fractal properties of ISSRs for different seasons suggest different formation processes. For this we might also take into account the seasonal fluctuation in the number of ISSRs with a peak in summer (in agreement with Reutter et al., 2020). A possible explanation is the transportation of water ~~vapour~~ vapor into the UTLS by convection during the summer months. A multitude of convection sites causes high ISSR numbers while the winter ~~month~~ months are dominated by low pressure areas and frontal systems. The ascending air flow of the warm conveyor belt causes a connected area of supersaturation. This hypotheses is supported by the shorter mean latitudinal and longitudinal spans in summer compared to winter months.

As a further corroboration we calculated the mean area of ISSRs from our statistics of number and area of ISSRs in Section 3.1, which is represented in Figure 15.

We clearly see a pronounced seasonal cycle in the mean area of ISSRs with a very distinct maximum in winter (mean values $\bar{A} \sim 5 - 6 \cdot 10^{11}\mathrm{m}^2$) and a clear minimum in summer (mean values $\bar{A} \sim 2.5 - 3 \cdot 10^{11}\mathrm{m}^2$); assuming a purely spherical shape, this would translate into a factor of 2 for the radii. This behavior is consistent with the proposed formation mechanisms: convective processes in summer produce more localized ISSRs, whereas large-scale dynamics in winter lead to more extended structures.

While the 200 hPa and 300 hPa levels show good agreement across all seasons, the average area per ISSR is noticeably larger at 250 hPa during summer. This feature does not represent an outlier but can be explained by jointly considering the number count and total area. In winter, both the number count and total area at 250 hPa are substantially lower than at 300 hPa. During summer, the total area at both levels becomes comparable, despite a lower number count at 250 hPa. Consequently, the ratio of total area to number count is increased at 250 hPa in summer. Seasonal variations in tropopause altitude primarily affect the 250 hPa level as it is intermittently located within both the upper troposphere and lower stratosphere. In contrast, 200 hPa remains predominantly above and 300 hPa predominantly below the tropopause throughout the year (Spichtinger et al., 2003a), resulting in less pronounced seasonal variability at those levels.

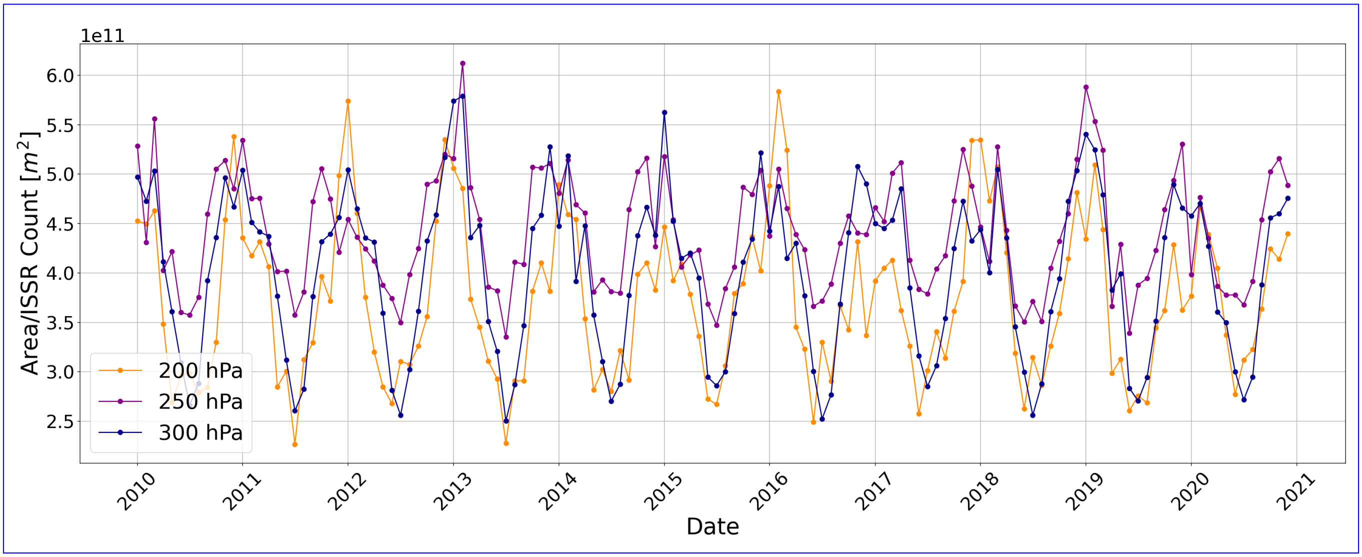

Figure 15. Averaged area as calculated from the number and areas of ISSRs, taken from the evaluation in section 3.1 using data with unfilled holes.

Extending this hypothesis to the seasonal variation in the fractal dimension, particularly during the period with the lowest values in summer, provides two possible interpretations. One perspective suggests that convective sites lead to ISSRs with frayed boundaries, resulting in long perimeters compared to the smoother edges of ISSRs caused by frontal activity, i.e. large scale dynamics. An alternative interpretation posits that multiple convective ”bubbles” occurring in close proximity may be collectively labeled as a single ISSR. This would lead to elevated perimeters attributed to their intricate structure and the added internal perimeter created by holes that segregate convective regions.

In addition, the scale break in the Weibull plots of the pathlengths also suggest a possible superposition of two different formation pathways. This can possibly originate in the slopes corresponding to smaller and larger ISSRs. Smaller scale ISSRs form in localized lifting phenomena as e.g. convection. Frontal activity and large scale dynamics create larger areas of supersaturation with respect to ice.

However, an in depth investigation of the formation processes of ISSRs for the full data set is beyond the scope of this study, but is planned as future investigation.

~~Ice supersaturated regions in the UTLS are important potential formwation regions of ice clouds and contrails, respectively. For a better understanding of these regions and thus a meaningful representation in models on different scales and resolutions, we investigated ISSRs in the ERA5 data as "macroscopic" and quasi two dimensional objects on pressure levels in the UTLS. Especially, a potential fractal characteristics is investigated. The analysis of the data with the examination of the area-perimeter relation revealed slopes equaling fractal dimensions, providing strong evidence of ISSRs in the UTLS being self-similar. The order of magnitude of the dimension values is reasonable as a value between 1 and 2 is expected for planar shapes with rough edges. Pathlengths were also investigated statistically, providing results consistent with the fractal properties. A seasonal cycle~~

~~could be found, showing smaller fractal dimensions during summer in agreement with smaller pathlength, and larger fractal dimensions with larger pathlengths during winter, respectively. The seasonal cycle also points to possible different formation processes, producing different fractal features. We hypothesized formation of ISSRs dominantly by convection during summer, and by large scale dynamics during winter season, corroborated by the distinct features of fractal dimensions, pathlengths, and even number of ISSRs. A scale break of pathlength statistics at about~~ $\sim 10^5$m ~~also suggested different formation processes. However, a detailed evaluation of these possible formation pathways is beyond the scope of this study.~~

~~The~~

5.3 Outlook

The impact and implications of these findings are broad. The level of self similarity across scales can prove helpful in modelling more accurate representations of ISSRs and can thus impact forecasts. Knowing that ISSRs largely keep their characteristics irrespective of their scale can simplify their modelling. The identification of fractal structures enriches scientific inquiry by providing new tools for analysis, enhancing modelling accuracy, and offering deeper insights into the complexity of natural phenomena. As a more practical aspect of the analysis, the fractal properties of ISSRs must be taken into account for the highly discussed concepts of contrail avoidance (e.g., Petzold et al., 2025). Looking at the examples of frayed ISSRs in Figs. 3 and 4, it seems to be very optimistic that contrail avoidance might work in a meaningful, impactful or feasable way; the large amount of small ISSRs (or short pathlengths) in connection with the huge fractal objects makes it very difficult to manage efficient contrail avoidance in the Northern hemisphere.

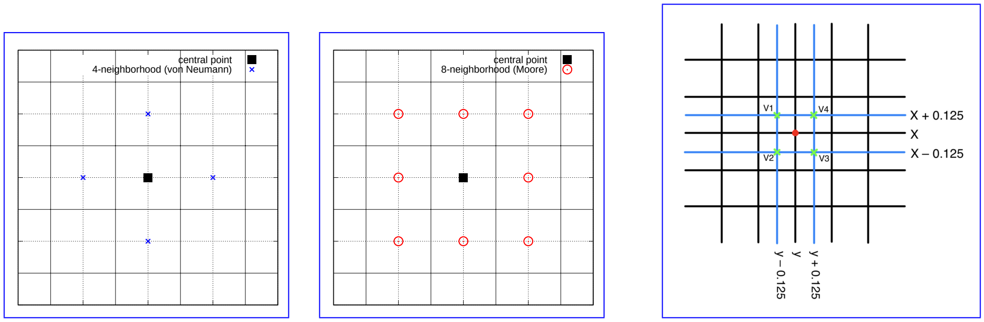

Figure A1. Two possible measures for connecting points on gridded data (Chopard and Droz, 1998). Black square: Center point. Left: Blue crosses indicate points connected to the central point using the 4-neighborhood (von Neumann neighborhood). Middle: Red circles indicate points connected to the central point using the 8-neighborhood (Moore neighborhood). Right: Assignment of area to a grid point, using a halo of ± 0.125 degrees.

Appendix A: Methods for evaluation

In Figure A1 two possible definitions of neighborhoods of points on gridded data are shown, originating from investigations with cellular automaton (Chopard and Droz, 1998). In case of a 4-neighborhood (or von Neumann neighborhood), the central pixel has only connection to pixels via the four edges of the point, whereas in case of a 8-neighborhood (or Moore neighborhood) the central pixel is additionally connected to pixels via the diagonals[1]. In our evaluation, we choose the Moore neighborhood, since the physical properties as connectivity should not depend on a grid representation, i.e. rotation of the object should result into the "same" connected object.

For the derivation of the grid point's area we use the coordinates of the point (x,y) as the center of a rectangular with vertices $(x \pm 0.125, y \pm 0.125)$ (see right panel of figure A1). The area (in square metres) is then assigned to the grid point, taking into account the latitudinal stretching of the grid. For the derivation of the perimeter, we use the four edges of the introduced rectangular, with the respective length (in metres). If there is no neighboring grid with index=1, the edge is counted as part of the perimeter.

Appendix B: Changes in fractal dimensions

In this appendix we illustrate some effects which might have some influence on the change in the fractal dimension. ~~As a first example, we compare the fractal dimensions of a 2D sphere with a systematically distorted ellipse.~~ We use the area-perimeter relation $P = CA^{\frac{D}{2}}$ for the investigations.

For geometric objects, the fractal dimension coincides with the classical integer values dimension, as can be seen directly for simple examples as spheres, squares, rectangulars with fixed ratio of sides.

[1] In the description of the used program package, the 4-neighborhood is called 1-connectivity, and the 8-neighborhood is called 2-connectivity. In fact, in literature these terms are not frequently used.

1. Sphere: For a sphere ~~we can determine the~~ with radius r we easily calculate the perimeter $P = 2\pi r$ and the area $A = \pi r^2$, thus leading to the derivation $2\pi r = P = CA^{\frac{D}{2}} = C\left(\pi r^2\right)^{\frac{D}{2}} = C\pi^{\frac{D}{2}} r^D$ which immediately gives $D = 1$ and $C = 2\sqrt{\pi}$.

2. Rectangular with fixed ratio of sides: We assume sides a and $b = d \cdot a$ with a fixed value $d > 0$; thus, we calculate $2(1+d)a = P = CA^{\frac{D}{2}} = C\left(d \cdot a^2\right)^{\frac{D}{2}} = Cd^{\frac{D}{2}} a^D$ with $D = 1$ and $C = \frac{2(1+d)}{\sqrt{d}}$. Note that the case of a square ($d = 1$) is included here, leading to $C = 4$.

As a first example for a fractal object, we compare the fractal dimension of a square with a systematically stretched rectangular, i.e. we change the ratio between the two sides, while we proceed to larger sizes. In fact, we set $a = \epsilon$ and $b = \epsilon^2$ for $\epsilon \in \mathbb{R}_+$. Thus, we can calculate

$$A = a \cdot b = \epsilon^3, \quad P = 2a + 2b = 2\epsilon + 2\epsilon^2 = 2\epsilon(1+\epsilon) \tag{B1}$$

leading to the area-perimeter ~~relation analytically, i.e. with $A = \pi r^2$ and $P = 2r\pi$ we obtain $A = C \cdot P^2$ with a constant $C = \frac{1}{4\pi}$ and a "fractal"~~ relation

$$2\epsilon(1+\epsilon) = P = CA^{\frac{D}{2}} = C\left(\epsilon^3\right)^{\frac{D}{2}}. \tag{B2}$$

Applying the logarithm, we can derive an approximate value of the dimension ~~$\alpha_K = 2$. For our ellipses we prescribe one half axis a and determine the other half axis as $b = a^2$. Using a simple simulation on a 2D rectangulargrid we can use a scatter plot of data points to determine the fractal dimension of the ellipse as $\alpha_E \sim 1.52$.Both cases, spheres and ellipses are shown in the~~ D (and also the constant C).
Using $\log(P) = \log(2) + \log(\epsilon) + \log(1+\epsilon)$, and $\log(A) = 3\log(\epsilon)$, we obtain for the dimension

$$\frac{D}{2} = \frac{\log(P) - \log(C)}{\log(A)} = \frac{\log(2) + \log(\epsilon) + \log(1+\epsilon) - \log(C)}{3\log(\epsilon)} \tag{B3}$$

For large ϵ we find $\log(1+\epsilon) \approx \log(\epsilon)$ and $\log(P) - \log(C) \approx \log(P)$, thus we find

$$\frac{D}{2} = \lim_{\epsilon \to \infty} \frac{\log(P) - \log(C)}{\log(A)} = \frac{2}{3} \Leftrightarrow D = \frac{4}{3}, \tag{B4}$$

and we also obtain $C \approx 2$. In the left panel of ~~figure B1 . Thus, systematically elongated ellipses turn more to a~~ Figure B1 the area-perimeter relation for a square and a stretched rectangular are shown together with the theoretically derived values for the fits. The systematically stretched rectangular turns into a more line-shaped geometric object, thus changing the fractal dimension to ~~smaller~~ larger values.

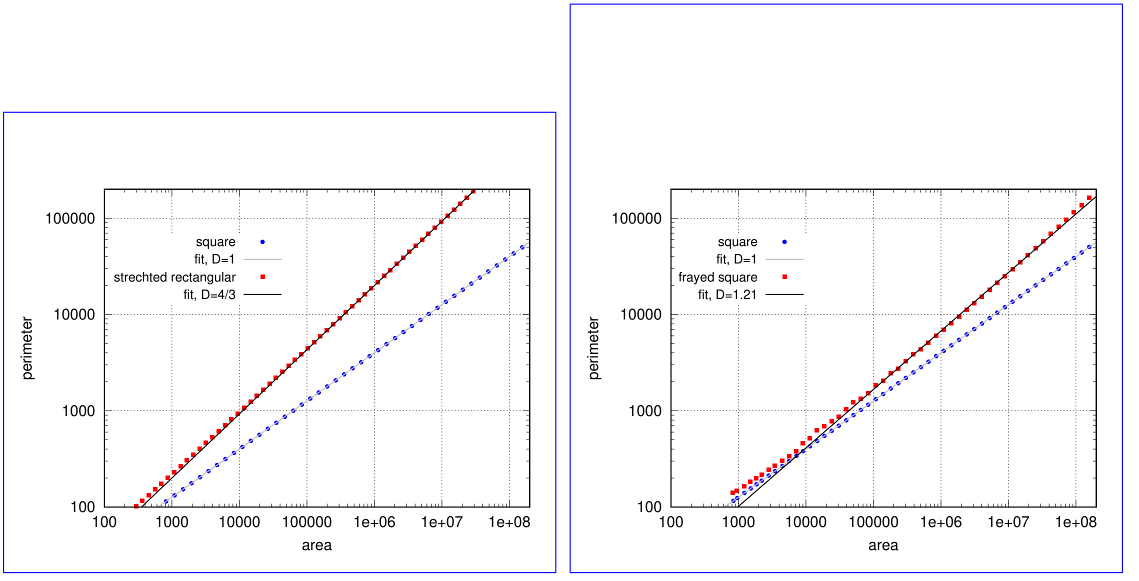

Figure B1. Examples of fractal dimension for 2D objects. Left: square vs. stretched rectangular. Right: square vs. frayed square. The fractal dimension of the frayed square is determined using linear regression to the data points in logarithmic scale. The fits to the other objects are based on the theoretically obtained values.

As a second example, we investigate the case of a square, which boundary is systematically frayed, thus leading to a slightly smaller area but to a strongly enhanced perimeter. Again, for a normal square we would find a ~~fractal dimension of~~ $\cancel{\alpha_S = 2}$(fractal) dimension of $D = 1$. However, for the frayed square, we see that the fractal dimension is also ~~reduced~~enhanced, leading to values of about $\cancel{\alpha_{FS} \sim 1.6}$$D \sim 1.21$. The scatter plot of the normal square and the frayed square, respectively, is shown in the right panel of ~~figure~~Figure B1, together with the linear ~~fits~~ fit via regression. These two mechanisms (stretching and fraying) can for instance serve for changing fractal dimensions of ~~two dimensional~~ "two dimensional" geometric objects.

Appendix C: Changes due to coarsening of the grid

For a rigorous definition of fractal dimensions (in the Hausdorff sense) one would have to send the grid resolution to zero, i.e. approaching an infinitely small length scale for measuring perimeters and areas, respectively. Only in the limit, the fractal dimensions are well defined. We cannot obtain this limit, since we are limited by the highest resolution of the ERA5 data, which is $0.25° \times 0.25°$ on an isobar surface. However, we can check the robustness of the fractal properties by artificial coarsening of the data and redoing the evaluation in terms of calculating the fractal dimension for the coarser objects. For this purpose, we introduced two different data sets, i.e. a **coarse** set (half resolution, i.e. $0.5° \times 0.5°$), and a **very coarse** set (quarter resolution, i.e. $1° \times 1°$). In both cases, we use the same ERA5 data, i.e. a full set of 11 years (2010-2020).

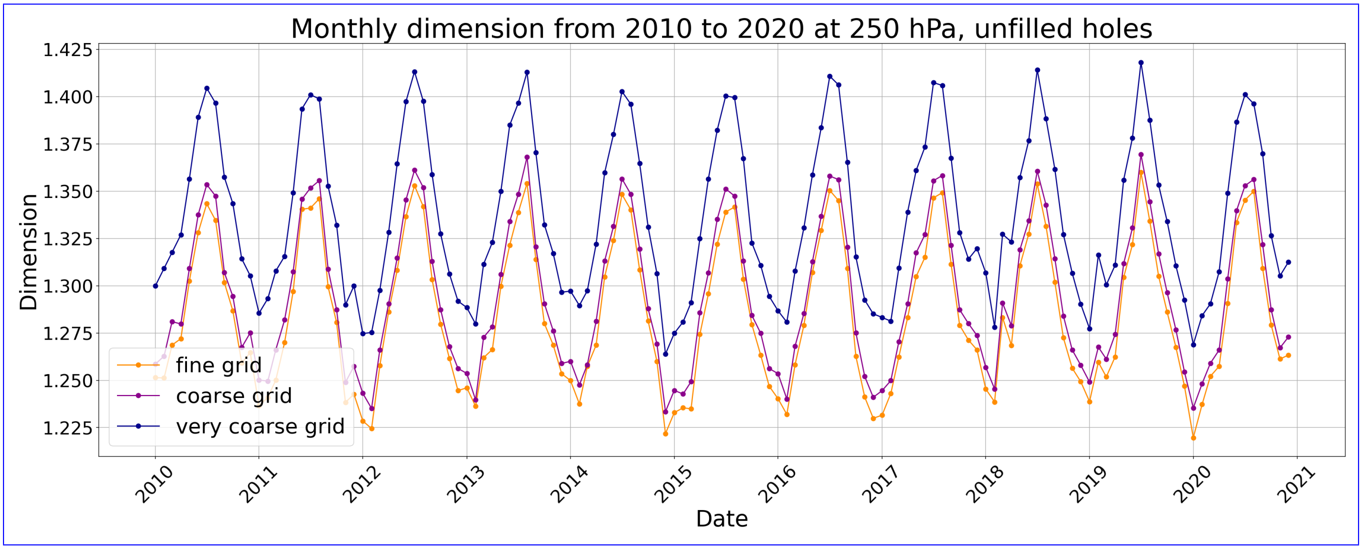

Figure C1. Fractal dimensions at pressure level $p = 250\,\mathrm{hPa}$ for different grid resolutions (fine $0.25° \times 0.25°$ in orange, coarse $0.5° \times 0.5°$ in violet, and very coarse $1° \times 1°$ in dark blue) in a monthly resolution for the time span of 11 years of ERA5 data.

In Figure C1 we exemplarily show the results for the pressure level $p = 250\,\mathrm{hPa}$; for the other two pressure levels we find qualitatively the same features (not shown). For all grid resolution we still find the signature of self-similarity, i.e. a fractal dimension of $D > 1$. There is a similar qualitative change if we proceed from coarser to finer grid resolution. The highest values of D are found for the very coarse resolution, with a jump in order of $\Delta D \sim 0.04 - 0.06$ to the coarse resolution. The next step to the fine (i.e. ERA5 native) resolution is then much smaller, the difference is in order of $\Delta D \sim 0.01 - 0.02$. More precisely, the dimension seem to "converge" to the values of the fine resolution, although this statement is only qualitatively, based on 3 available grid resolution. For the other pressure levels, we find the same qualitative behavior, and also the values of the difference in D are almost the same.

Thus, we can conclude that the fractal properties seem to be robust over all tested grid resolutions. Surprisingly, the highest values of the fractal dimension can be obtained for the coarsest resolution of $1° \times 1°$, whereas the self-similarity is still prominent for the ERA5 resolution. Finally, we can state that the behavior is exactly the same for the filled versions of ISSR, as described in the previous section 3.3.

Appendix D: Potential errors for gridded data: Overestimation of perimeters

It is well known that the calculation of perimeter on gridded data lead to overestimation of this quantity (Imre, 2006). However, it is not completely clear, if and how the area-perimeter relation might change due to this error. Exemplarily, we investigate this for a sphere; we calculate the area and perimeter according to the methods explained above and compare these values with the analytically calculated quantities. The area-perimeter relations are represented in ~~figure~~Figure D1

Although there is a systematic shift in perimeters, the resulting fractal dimension ~~$\alpha \sim 1.997$~~ $D \sim 0.999564$ (as a linear fit to the double logarithmic scatter plot) is very close to the analytically determined ~~fractal dimension $\alpha = 2$~~"fractal" dimension $D = 1$. Thus, we are ~~quite~~ confident that the systematic overestimation of perimeters does not disturb the quantitative investigations of area-perimeter relations.

Appendix E: Weibull plots

Here we give a short explanation for the use of the Weibull plot. The general form of a Weibull probability distribution of a non-negative random variable x is given by

$$f(x) = \gamma p x^{p-1} \exp(-\gamma x^p) \tag{E1}$$

with the shape parameter $p \in \mathbb{R}_+$, responsible for the slope of the distribution, and the scale parameter $\gamma \in \mathbb{R}$~~, respectively~~. The cumulative distribution (i.e. via integration) can be written as

$$F(x) = 1 - \exp(-\gamma x^p), \text{ i.e. } 0 \leq F(x) \leq 1. \tag{E2}$$

This equation can be reformulated as follows.

$$1 - F(x) = \exp(-\gamma x^p) \quad \Leftrightarrow \quad \frac{1}{1-F(x)} = \exp(\gamma x^p) \tag{E3}$$

$$\Leftrightarrow \quad \log\left(\frac{1}{1-F(x)}\right) = \gamma x^p \tag{E4}$$

$$\Leftrightarrow \quad \log\left(\log\left(\frac{1}{1-F(x)}\right)\right) = \log(\gamma x^p) \tag{E5}$$

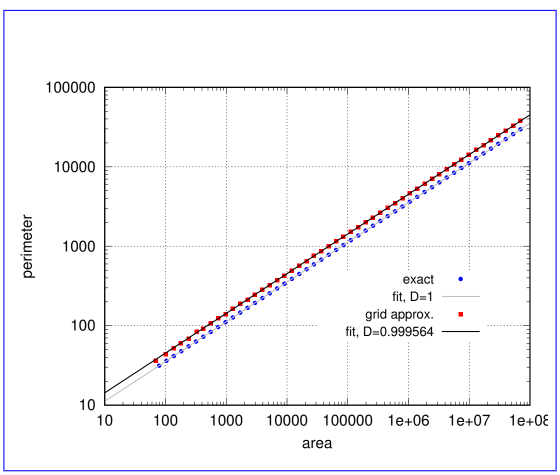

Figure D1. Systematic error for determining perimeters of spheres on gridded data. Blue circles indicate the exact values (with a fractal dimension $D = 1$), red squares indicate the numerically derived values (with a fractal dimension $D = 0.999564$). The dimensions were obtained using a linear regression to the data points in logarithmic scale.

Finally, we end with this equation

$$\log\left(\log\left(\frac{1}{1-F(x)}\right)\right) = \log(\gamma) + p\cdot\log(x) \tag{E6}$$

thus constituting a linear relationship between the quantities $\eta := \log(-\log(1-F(x)))$ and $\xi = \log(x)$ with a slope of p. Thus, using a scatter plot of variables (ξ,η) we can derive the parameter p via linear regression.

Appendix F: Fractal dimension - additional plots

Here we present the determination of the fractal dimension for three pressure levels in case of July 2020.

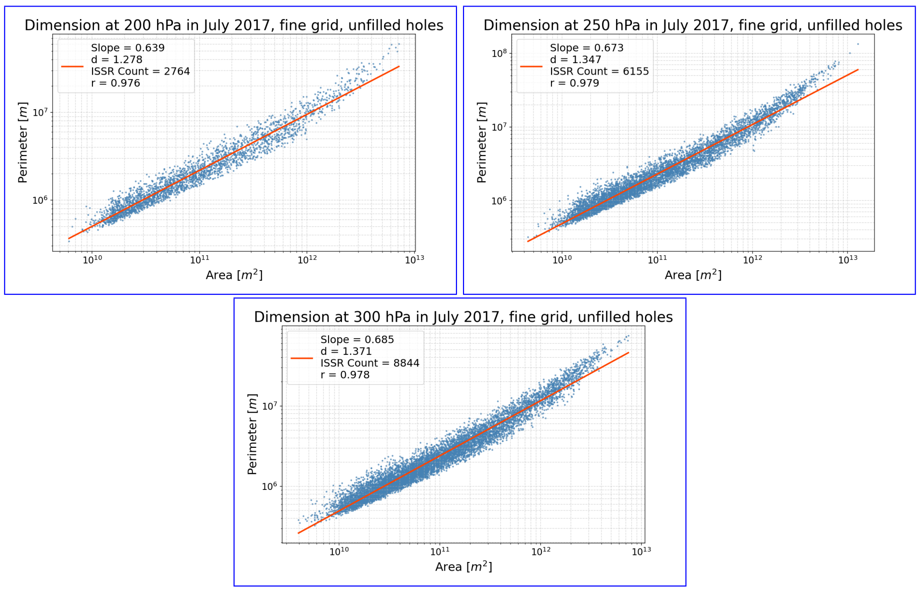

Figure F1. Determination of the fractal dimension via fits to the area-perimeter relation (eq. 4) in case of July 2017. Blue dots indicate the data points (A,P), red lines are the fits from linear regression. Left: Pressure level $p = 200\,\mathrm{hPa}$; Middle: Pressure level $p = 250\,\mathrm{hPa}$; Right: Pressure level $p = 300\,\mathrm{hPa}$

Appendix G: Results using filled holes

In this appendix, we present the corresponding figures based on the data set with filled holes. These results complement the analysis shown in the main text, where primarily the unfilled-hole data were discussed.

The purpose of including the filled-hole data is to demonstrate the robustness of the identified statistical characteristics of ISSR horizontal extensions with respect to the treatment of internal gaps. While minor quantitative differences may occur, the overall behavior of the distributions, including their seasonal dependence and characteristic regimes, remains consistent.

The following figures therefore provide a direct comparison to the results presented in Sections 4.1 and 4.2.

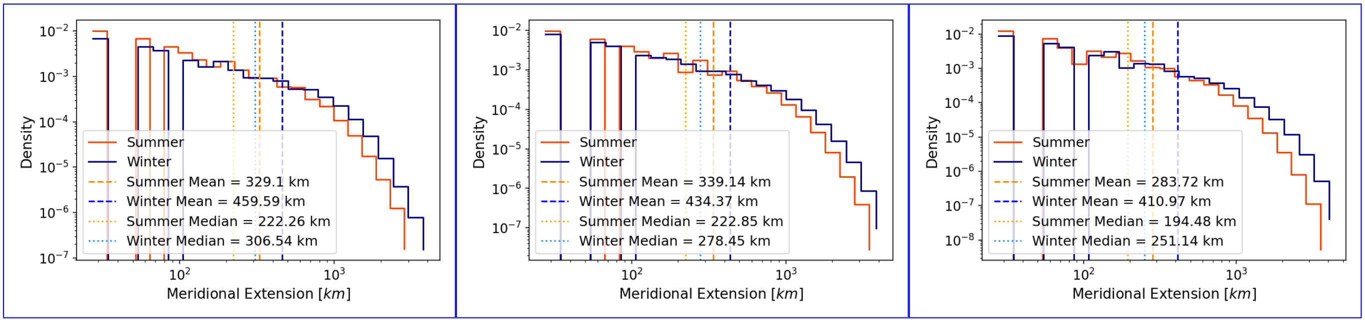

Figure G1. Distributions of meridional span (i.e. pathlengths in North-South direction) for different seasons, i.e. summer (JJA, orange colors) and winter (DJF, blue colors) using data with filled holes. Mean values are indicated by vertical dashed lines, median values are indicated by vertical dotted lines. Left: $200\,\mathrm{hPa}$, Middle: $250\,\mathrm{hPa}$, Right: $300\,\mathrm{hPa}$

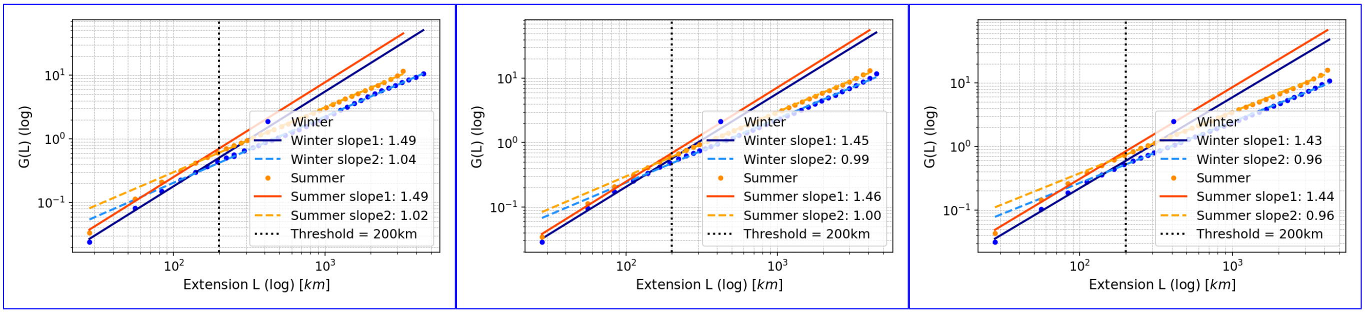

Figure G2. Weibull plots for the pathlength distributions in North-South direction using data with filled holes. The linear regression fit is shown for the regimes of pathlengths smaller and larger than $\sim 2 \cdot 10^2 \mathrm{km}$, this threshold being indicated by a dotted line. Blue/orange colors indicate winter/summer data, respectively. The fits to the different regimes are represented by a dashed and a solid line. Left: $200\,\mathrm{hPa}$, Middle: $250\,\mathrm{hPa}$, Right: $300\,\mathrm{hPa}$

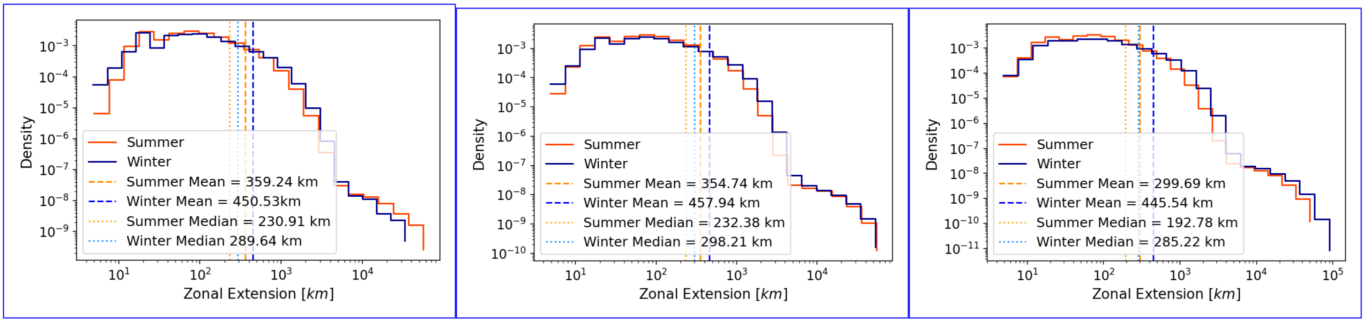

Figure G3. Distributions of zonal span (i.e. pathlengths in East-West direction) for different seasons, i.e. summer (JJA, orange colors) and winter (DJF, blue colors) using data with filled holes. Mean values are indicated by vertical dashed lines, median values are indicated by vertical dotted lines. Left: $200\,\mathrm{hPa}$, Middle: $250\,\mathrm{hPa}$, Right: $300\,\mathrm{hPa}$

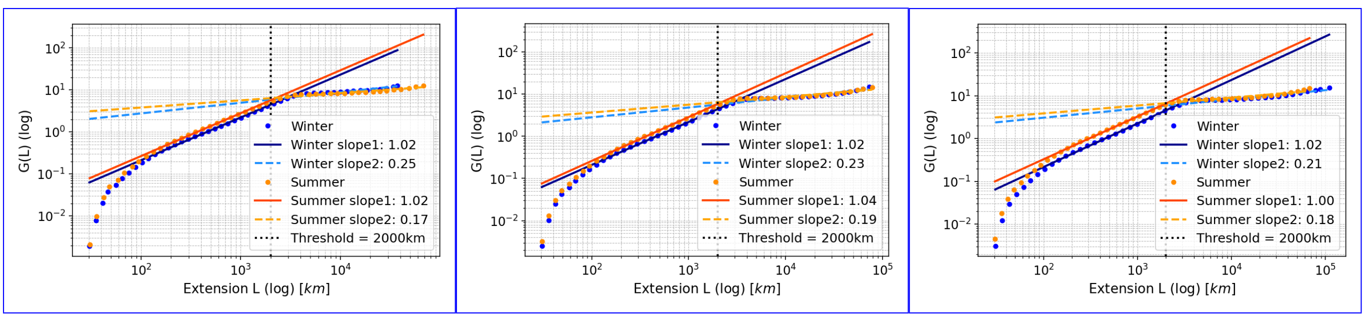

Figure G4. Weibull plots for the pathlength distributions in East-West direction using data with filled holes. The linear regression fit is shown for the regimes of pathlengths smaller and larger than $\sim 2 \cdot 10^3 \mathrm{km}$, this threshold being indicated by a dotted line. Blue/orange colors indicate winter/summer data, respectively. The fits to the different regimes are represented by a dashed and a solid line. Left: $200\,\mathrm{hPa}$, Middle: $250\,\mathrm{hPa}$, Right: $300\,\mathrm{hPa}$

. The code for evaluation is available at Zenodo. DOI: 10.5281/zenodo.15531354

. The ERA5 data are available at the MARS archive of ECMWF.

. HS and PS designed the study. HS and SN developed the data evaluation methods, HS carried out the data analysis. HS, PS and PR discussed the results, and wrote the manuscript.

. The authors state that there are no competing interests.

. We thank two anonymous reviewers for important comments leading to an overall improvement of the manuscript. Philipp Reutter acknowledges support by the DFG within the Transregional Collaborative Research Centre TRR301 TPChange, Project-ID 428312742 , project C01. Peter Spichtinger acknowledges support by the DFG within the Transregional Collaborative Research Centre TRR301 TPChange, Project-ID 428312742, project B07. The study contributes to the project "Big Data in Atmospheric Physics (BINARY)", funded by the Carl Zeiss Foundation (grant P2018-02-003).

References

Batista-Tomás, A., Díaz, O., Batista-Leyva, A., and Altshuler, E.: Classification and dynamics of tropical clouds by their fractal dimension, Quarterly Journal of the Royal Meteorological Society, 142, 983–988, https://doi.org/10.1002/qj.2699, 2016.

Benner, T. and Curry, J.: Characteristics of small tropical cumulus clouds and their impact on the environment, Journal of Geophysical Research-Atmospheres, 103, 28 753–28 767, https://doi.org/10.1029/98JD02579, 1998.

Brinkhoff, L. A., von Savigny, C., Randall, C. E., and Burrows, J. P.: The fractal perimeter dimension of noctilucent clouds: Sensitivity analysis of the area-perimeter method and results on the seasonal and hemispheric dependence of the fractal dimension, Journal of Atmospheric and Solar-Terrestrial Physics, 127, 66–72, https://doi.org/10.1016/j.jastp.2014.06.005, 2015.

Cahalan, R. and Joseph, J.: Fractal Statistics Of Cloud Fields, Monthly Weather Review, 117, 261–272, https://doi.org/10.1175/1520-0493(1989)117<0261:FSOCF>2.0.CO;2, 1989.

Cahalan, R., Ridgway, W., Wiscombe, W., Bell, T., and Snider, J.: The Albedo of Fractal Stratocumulus Clouds, Journal of the Atmospheric Sciences, 51, 2434–2455, https://doi.org/10.1175/1520-0469(1994)051<2434:TAOFSC>2.0.CO;2, 1994.

Cheng, Q.: The perimeter-area fractal model and its application to geology, Mathematical Geology, 27, 69–82, https://doi.org/10.1007/BF02083568, 1995.

Chopard, B. and Droz, M.: Cellular Automata Modeling of Physical Systems, Collection Alea-Saclay: Monographs and Texts in Statistical Physics, Cambridge University Press, https://doi.org/https://doi.org/10.1017/CBO9780511549755, 1998.

Christensen, H. M. and Driver, O. G. A.: The Fractal Nature of Clouds in Global Storm-Resolving Models, Geophysical Research Letters, 48, https://doi.org/10.1029/2021GL095746, 2021.

Clough, S. A., Iacono, M. J., and Moncet, J.: Line-by-line calculations of atmospheric fluxes and cooling rates: Application to water vapor, Journal of Geophysical Research: Atmospheres, 97, 15 761–15 785, https://doi.org/10.1029/92JD01419, 1992.

Dessler, A. E. and Sherwood, S. C.: A matter of humidity, Science, 323, 1020–1021, https://doi.org/10.1126/science.1171264, 2009.

DeWitt, T. D., Garrett, T. J., Rees, K. N., Bois, C., Krueger, S. K., and Ferlay, N.: Climatologically invariant scale invariance seen in distributions of cloud horizontal sizes, Atmospheric Chemistry and Physics, 24, 109–122, https://doi.org/10.5194/acp-24-109-2024, 2024.

Diao, M., Zondlo, M. A., Heymsfield, A. J., Avallone, L. M., Paige, M. E., Beaton, S. P., Campos, T., and Rogers, D. C.: Cloud-scale ice-supersaturated regions spatially correlate with high water vapor heterogeneities, Atmospheric Chemistry and Physics, 14, 2639–2656, https://doi.org/10.5194/acp-14-2639-2014, 2014.

Florio, B. J., Fawell, P. D., and Small, M.: The use of the perimeter-area method to calculate the fractal dimension of aggregates, Powder Technology, 343, 551–559, https://doi.org/10.1016/j.powtec.2018.11.030, 2019.

Fusina, F., Spichtinger, P., and Lohmann, U.: Impact of ice supersaturated regions and thin cirrus on radiation in the midlatitudes, Journal of Geophysical Research: Atmospheres, 112, https://doi.org/10.1029/2007JD008449, 2007.

Gettelman, A., Fetzer, E. J., Eldering, A., and Irion, F. W.: The Global Distribution of Supersaturation in the Upper Troposphere from the Atmospheric Infrared Sounder, Journal of Climate, 19, 6089 – 6103, https://doi.org/10.1175/JCLI3955.1, 2006.

Gierens, K. and Spichtinger, P.: On the size distribution of ice-supersaturated regions in the upper troposphere and lowermost stratosphere, in: Annales Geophysicae, vol. 18, pp. 499–504, Springer, https://doi.org/10.1127/0941-2948/2002/0011-0083, 2000.

Gotoh, K. and Fujii, Y.: A fractal dimensional analysis on the cloud shape parameters of cumulus over land, Journal of applied meteorology, 37, 1283–1292, https://doi.org/10.1175/1520-0450(1998)037<1283:AFDAOT>2.0.CO;2, 1998.

Haywood, J. M., Allan, R. P., Bornemann, J., Forster, P. M., Francis, P. N., Milton, S., Rädel, G., Rap, A., Shine, K. P., and Thorpe, R.: A case study of the radiative forcing of persistent contrails evolving into contrail-induced cirrus, Journal of Geophysical Research: Atmospheres, 114, https://doi.org/10.1029/2009JD012650, 2009.

Held, I. M. and Soden, B. J.: Water vapor feedback and global warming, Annual review of energy and the environment, 25, 441–475, https://doi.org/10.1146/annurev.energy.25.1.441, 2000.

Hersbach, H., Bell, B., Berrisford, P., Hirahara, S., Horányi, A., Muñoz-Sabater, J., Nicolas, J., Peubey, C., Radu, R., Schepers, D., Simmons, A., Soci, C., Abdalla, S., Abellan, X., Balsamo, G., Bechtold, P., Biavati, G., Bidlot, J., Bonavita, M., Chiara, G., Dahlgren, P., Dee, D., Diamantakis, M., Dragani, R., Flemming, J., Forbes, R., Fuentes, M., Geer, A., Haimberger, L., Healy, S., Hogan, R. J., Hólm, E., Janisková, M., Keeley, S., Laloyaux, P., Lopez, P., Lupu, C., Radnoti, G., Rosnay, P., Rozum, I., Vamborg, F., Villaume, S., and Thépaut, J.: The ERA5 global reanalysis, Quarterly Journal of the Royal Meteorological Society, 146, 1999–2049, https://doi.org/10.1002/qj.3803, 2020.

Imre, A.: Artificial fractal dimension obtained by using perimeter-area relationship on digitalized images, Applied Mathematics and Computation, 173, 443–449, https://doi.org/10.1016/j.amc.2005.04.042, 2006.

Joseph, J. and Cahalan, R.: Nearest Neighbor Spacing of Fair Weather Cumulus Clouds, Journal of Applied Meteorology, 29, 793–805, https://doi.org/10.1175/1520-0450(1990)029<0793:NNSOFW>2.0.CO;2, 1990.

Klinkenberg, B.: A review of methods used to determine the fractal dimension of linear features, Mathematical Geology, 26, 23–46, https://doi.org/10.1007/BF02065874, 1994.

Köhler, D., Reutter, P., and Spichtinger, P.: Relative humidity over ice as a key variable for Northern Hemisphere midlatitude tropopause inversion layers, Atmospheric Chemistry and Physics, 24, 10 055–10 072, https://doi.org/10.5194/acp-24-10055-2024, 2024.

Krämer, M., Rolf, C., Luebke, A., Afchine, A., Spelten, N., Costa, A., Meyer, J., Zoeger, M., Smith, J., Herman, R. L., et al.: A microphysics guide to cirrus clouds – Part 1: Cirrus types, Atmospheric Chemistry and Physics, 16, 3463–3483, https://doi.org/10.5194/acp-16-3463-2016, 2016.

Lamquin, N., Stubenrauch, C. J., Gierens, K., Burkhardt, U., and Smit, H.: A global climatology of upper-tropospheric ice supersaturation occurrence inferred from the Atmospheric Infrared Sounder calibrated by MOZAIC, Atmos. Chem. Phys., 12, 381–405, https://doi.org/10.5194/acp-12-381-2012, 2012.

Lee, D., Pitari, G., Grewe, V., Gierens, K., Penner, J., Petzold, A., Prather, M., Schumann, U., Bais, A., Berntsen, T., Iachetti, D., Lim, L., and Sausen, R.: Transport impacts on atmosphere and climate: Aviation, Atmospheric Environment, 44, 4678–4734, https://doi.org/https://doi.org/10.1016/j.atmosenv.2009.06.005, transport Impacts on Atmosphere and Climate: The ATTICA Assessment Report, 2010.

Lee, D., Fahey, D., Skowron, A., Allen, M., Burkhardt, U., Chen, Q., Doherty, S., Freeman, S., Forster, P., Fuglestvedt, J., Gettelman, A., De León, R., Lim, L., Lund, M., Millar, R., Owen, B., Penner, J., Pitari, G., Prather, M., Sausen, R., and Wilcox, L.: The contribution of global aviation to anthropogenic climate forcing for 2000 to 2018, Atmospheric Environment, 244, 117 834, https://doi.org/https://doi.org/10.1016/j.atmosenv.2020.117834, 2021.

Lovejoy, S.: Area-perimeter relation for rain and cloud areas, Science, 216, 185–187, https://doi.org/10.1126/science.216.4542.185, 1982.

Lovejoy, S. and Mandelbrot, B. B.: Fractal properties of rain, and a fractal model, Tellus A, 37A, 209–232, https://doi.org/10.1111/j.1600-0870.1985.tb00423.x, 1985.

Mandelbrot, B.: The Fractal Geometry of Nature, W. H. Freeman and Co., ISBN 0-7167-1186-9, 1982.

Mandelbrot, B. B., Passoja, D. E., and Paullay, A. J.: Fractal character of fracture surfaces of metals, Nature, 308, 721–722, https://doi.org/10.1038/308721a0, 1984.

Marenco, A., Thouret, V., Nédélec, P., Smit, H., Helten, M., Kley, D., Karcher, F., Simon, P., Law, K., Pyle, J., et al.: Measurement of ozone and water vapor by Airbus in-service aircraft: The MOZAIC airborne program, An overview, Journal of Geophysical Research: Atmospheres, 103, 25 631–25 642, https://doi.org/10.1029/98JD00977, 1998.

Murphy, D. M. and Koop, T.: Review of the vapour pressures of ice and supercooled water for atmospheric applications, Quarterly Journal of the Royal Meteorological Society, 131, 1539–1565, https://doi.org/10.1256/qj.04.94, 2005.

Peitgen, H.-O., Jürgens, H., and Saupe, D.: Chaos and fractals - new frontiers of science (2. ed.), Springer, ISBN 978-0-387-20229-7, https://doi.org/10.1007/b97624, 2004.

Petzold, A., Thouret, V., Gerbig, C., Zahn, A., Brenninkmeijer, C. A. M., Gallagher, M., Hermann, M., Pontaud, M., Ziereis, H., Boulanger, D., Marshall, J., Nédélec, P., Smit, H. G. J., Friess, U., Flaud, J.-M., Wahner, A., Cammas, J.-P., Volz-Thomas, A., and Team, I.: Global-scale atmosphere monitoring by in-service aircraft–current achievements and future prospects of the European Research Infrastructure IAGOS, Tellus B: Chemical and Physical Meteorology, 67, 28 452, https://doi.org/10.3402/tellusb.v67.28452, 2015.

Petzold, A., Neis, P., Rütimann, M., Rohs, S., Berkes, F., Smit, H. G. J., Krämer, M., Spelten, N., Spichtinger, P., Nédélec, P., and Wahner, A.: Ice-supersaturated air masses in the northern mid-latitudes from regular in situ observations by passenger aircraft: vertical distribution, seasonality and tropospheric fingerprint, Atmospheric Chemistry and Physics, 20, 8157–8179, https://doi.org/10.5194/acp-20-8157-2020, 2020.

Petzold, A., Khan, N. F., Li, Y., Spichtinger, P., Rohs, S., Crewell, S., Wahner, A., and Kramer, M.: Most long-lived contrails form within cirrus clouds with uncertain climate impact, Nature Communications, 16, https://doi.org/10.1038/s41467-025-65532-2, 2025.

Rees, K. N., Garrett, T. J., DeWitt, T. D., Bois, C., Krueger, S. K., and Riedi, J. C.: A global analysis of the fractal properties of clouds revealing anisotropy of turbulence across scales, Nonlinear Processes in Geophysics, 31, 497–513, https://doi.org/10.5194/npg-31-497-2024, 2024.

Reutter, P., Neis, P., Rohs, S., and Sauvage, B.: Ice supersaturated regions: properties and validation of ERA-Interim reanalysis with IAGOS in situ water vapour measurements, Atmospheric chemistry and physics, 20, 787–804, https://doi.org/10.5194/acp-20-787-2020, 2020.

Richardson, L. F.: Atmospheric diffusion shown on a distance-neighbour graph, Proceedings of the Royal Society of London. Series A, Containing Papers of a Mathematical and Physical Character, 110, 709–737, https://doi.org/10.1098/rspa.1926.0043, 1926.

Riese, M., Ploeger, F., Rap, A., Vogel, B., Konopka, P., Dameris, M., and Forster, P.: Impact of uncertainties in atmospheric mixing on simulated UTLS composition and related radiative effects, Journal of Geophysical Research: Atmospheres, 117, 2012.

Rys, F. and Waldvogel, A.: Fractal Shape Of Hail Clouds, Physical Review Letters, 56, 784–787, https://doi.org/10.1103/PhysRevLett.56.784, 1986.

Sakellariou, M., Nakos, B., and Mitsakaki, C.: On the fractal character of rock surfaces, in: International journal of rock mechanics and mining sciences & geomechanics abstracts, vol. 28, pp. 527–533, Pergamon, https://doi.org/https://doi.org/10.1016/0148-9062(91)91129-F, 1991.

Sanchez, N., Alfaro, E., and Pérez, E.: The fractal dimension of projected clouds, Astrophysical Journal, 625, 849–856, https://doi.org/10.1086/429553, 2005.

Schumann, U.: On conditions for contrail formation from aircraft exhausts, Meteorologische Zeitschrift, 5, 4–23, https://doi.org/10.1127/metz/5/1996/4, 1996.

Siebesma, A. and Jonker, H.: Anomalous scaling of cumulus cloud boundaries, Physical Review Letters, 85, 214–217, https://doi.org/10.1103/PhysRevLett.85.214, 2000.

Snow, A. D., Whitaker, J., Cochran, M., Miara, I., den Bossche, J. V., Mayo, C., Lucas, G., Cochrane, P., de Kloe, J., Karney, C., Shaw, J. J., Anh, T. Q., Filipe, Ouzounoudis, G., Dearing, J., Lostis, G., Couwenberg, B., Hoese, D., de Bittencourt, H., Little, B., May, R., Itkin, M., McDonald, D., Schneck, C., Gohlke, C., Jurd, B., Raspaud, M., Brett, M., and Meulien, M.: pyproj4/pyproj: 3.7.1 Release, https://doi.org/10.5281/zenodo.14876934, 2025.

Sornette, D.: Critical phenomena in natural sciences: chaos, fractals, selforganization and disorder: concepts and tools, Springer Science & Business Media, 2006.

Spichtinger, P. and Leschner, M.: Horizontal scales of ice-supersaturated regions, Tellus B: Chemical and Physical Meteorology, 68, 29 020, https://doi.org/10.3402/tellusb.v68.29020, 2016.

Spichtinger, P., Gierens, K., Leiterer, U., and Dier, H.: Ice supersaturation in the tropopause region over Lindenberg, Germany, Meteorologische Zeitschrift, 12, 143–156, https://doi.org/10.1127/0941-2948/2003/0012-0143, 2003a.

Spichtinger, P., Gierens, K., and Read, W.: The global distribution of ice-supersaturated regions as seen by the Microwave Limb Sounder, Quarterly Journal of the Royal Meteorological Society, 129, 3391–3410, https://doi.org/10.1256/qj.02.141, 2003b.

Sreenivasan, K.: Fractals And Multifractals In Fluid Turbulence, Annual Review Of Fluid Mechanics, 23, 539+, https://doi.org/https://doi.org/10.1146/annurev.fl.23.010191.002543, 1991.

Sreenivasan, K. and Meneveau, C.: The fractal facets of turbulence, Journal of Fluid Mechanics, 173, 357–386, https://doi.org/10.1017/S0022112086001209, 1986.

Stuber, N., Forster, P., Rädel, G., and Shine, K.: The importance of the diurnal and annual cycle of air traffic for contrail radiative forcing, Nature, 441, 864–867, https://doi.org/10.1038/nature04877, 2006.

Vogelaar, M. and Wakker, B.: Measuring the fractal structure of interstellar clouds, Astronomy and Astrophysics (ISSN 0004-6361), vol. 291, no. 2, p. 557-568, 291, 557–568, https://doi.org/10.1007/978-94-011-3384-5_90, 1994.

von Savigny, C., Brinkhoff, L. A., Bailey, S. M., Randall, C. E., and Russell III, J. M.: First determination of the fractal perimeter dimension of noctilucent clouds, Geophysical Research Letters, 38, https://doi.org/https://doi.org/10.1029/2010GL045834, 2011.

Wegener, A.: Über die Eisphase des Wasserdampfes in der Atmosphäre (On the ice phase of water vapor in the atmosphere), Meteor. Z., 27, 451–459, 1910.

Wegener, A.: Thermodynamik der Atmosphäre, J. A. Barth, Leipzig, 1911.